Journal of the Mechanics and Physics of Solids 109 (2017) 50–77

Contents lists available at ScienceDirect

Journal of the Mechanics and Physics of Solids

journal homepage: www.elsevier.com/locate/jmps

A finite difference method for off-fault plasticity throughout the earthquake cycle

Brittany A. Erickson[a,*], Eric M. Dunham[b,c], Arash Khosravifar[d]

[a] Department of Mathematics and Statistics, Portland State University, Portland, OR 97201, USA
[b] Department of Geophysics, Stanford University, Stanford, CA, USA
[c] Institute for Computational & Mathematical Engineering, Stanford University, Stanford, CA, USA
[d] Department of Civil and Environmental Engineering, Portland State University, Portland, OR, USA

ARTICLE INFO

Article history:
Received 9 June 2017
Revised 3 August 2017
Accepted 3 August 2017
Available online 18 August 2017

Keywords:
Earthquake cycle
Plasticity
Drucker–Prager
Finite difference method

ABSTRACT

We have developed an efficient computational framework for simulating multiple earthquake cycles with off-fault plasticity. The method is developed for the classical antiplane problem of a vertical strike-slip fault governed by rate-and-state friction, with inertial effects captured through the radiation-damping approximation. Both rate-independent plasticity and viscoplasticity are considered, where stresses are constrained by a Drucker–Prager yield condition. The off-fault volume is discretized using finite differences and tectonic loading is imposed by displacing the remote side boundaries at a constant rate. Time-stepping combines an adaptive Runge–Kutta method with an incremental solution process which makes use of an elastoplastic tangent stiffness tensor and the return-mapping algorithm. Solutions are verified by convergence tests and comparison to a finite element solution. We quantify how viscosity, isotropic hardening, and cohesion affect the magnitude and off-fault extent of plastic strain that develops over many ruptures. If hardening is included, plastic strain saturates after the first event and the response during subsequent ruptures is effectively elastic. For viscoplasticity without hardening, however, successive ruptures continue to generate additional plastic strain. In all cases, coseismic slip in the shallow sub-surface is diminished compared to slip accumulated at depth during interseismic loading. The evolution of this slip deficit with each subsequent event, however, is dictated by the plasticity model. Integration of the off-fault plastic strain from the viscoplastic model reveals that a significant amount of tectonic offset is accommodated by inelastic deformation ($\sim$0.1 m per rupture, or $\sim$10% of the tectonic deformation budget).

1. Introduction

Field observations reveal regions of highly damaged rock (containing abundant microfractures) surrounding a fault core, which many attribute to thousands of years of seismogenic cycling during which earthquakes shatter the rocks in the vicinity of the fault (Ben-Zion and Sammis, 2011; Chester et al., 1993; Chester and Logan, 1986; Faulkner et al., 2010; Mitchell and Faulkner, 2009; Shipton et al., 2005). Understanding how an earthquake will propagate is intimately tied to the evolution of these damage zones. Important and unsolved problems include the relationship between the degree of off-fault yielding and

* Corresponding author.
E-mail address: berickson@pdx.edu (B.A. Erickson).

http://dx.doi.org/10.1016/j.jmps.2017.08.002
0022-5096/

mechanical properties of fault zone material, how damage zones evolve with increasing cumulative slip, and how damage zones affect subsequent rupture.

Current models for dynamic rupture have led to much insight into earthquake propagation, the generation of high-frequency ground motion, and the influence of plasticity on rupture propagation (Dunham et al., 2011a,b; Gabriel et al., 2013a,b; Kaneko and Fialko, 2011; Ma and Andrews, 2010; Shi and Day, 2013; Templeton and Rice, 2008; Xu et al., 2012; Xu et al., 2012b). Although the inclusion of a plastic material response has been shown to reduce stress and slip velocities at the rupture front to reasonable values, little work has been done to understand the evolution of a damage zone (and its impact on rupture) over multiple event sequences. In particular, most dynamic rupture models currently make the assumption of a uniform background stress and are limited to single-event simulations where rupture is artificially initiated via a stress perturbation imposed on the fault. Earthquake cycle models, on the other hand, generate self-consistent initial conditions because of their ability to handle varying time scales. Cycle models developed in the boundary integral or boundary element context were limited to simulations in a uniform, linear elastic whole- or half-space (Lapusta et al., 2000; Tullis et al., 2012). Recent developments, however, have shown how to incorporate more realistic features (material heterogeneities or inelastic deformation, for example) into the earthquake cycle framework (Aagaard et al., 2013; Allison and Dunham, 2017; Barbot et al., 2012; Erickson and Dunham, 2014; Johnson and Segall, 2004; Kaneko et al., 2011; Thompson and Meade, 2016).

In this work, we study the role of plasticity throughout the earthquake cycle. The computational method is developed for the classical antiplane problem of a vertical strike-slip fault governed by rate-and-state friction. The off-fault material is idealized as a Drucker–Prager elastic–plastic solid and stresses are constrained by a depth-dependent yield condition. Inertia is approximated with radiation damping. Within the context of a time-stepping method, we solve the resulting equilibrium equation (a nonlinear, elliptic partial differential equation) for the displacement increment.

Although computational plasticity is most commonly addressed in a finite element framework, we develop a finite difference method, as the latter is easy to program, efficient, and can be applied in a straightforward manner in order to obtain a numerical approximation to the solution (Scalerandi et al., 1999). Recent work in summation-by-parts finite difference methods has furnished high-order accurate schemes that enforce boundary and interface conditions in a stable manner (through the simultaneous-approximation-term technique) (Kreiss and Scherer, 1974; 1977; Nordström et al., 2007; Svärd and Nordström, 2014). These methods provide a framework for proving convergence for linear and nonlinear problems, which is fundamental in order to obtain credible numerical approximations. In this work, an initial analysis is done of the underlying continuum problem to show it satisfies an energy estimate (in this case, dissipation of mechanical energy in the absence of non-trivial boundary conditions or source terms). The computational method then provides a spatial discretization that mimics the energy estimate of the continuum problem and proves stability of the method.

The paper is organized as follows: in Section 2 we state the continuum problem solved in this work. A rate-and-state frictional fault is embedded in an elastoplastic solid and the equation for static equilibrium is solved within the context of a time-stepping method that imposes remote loading and fault slip (in a manner consistent with a fault friction law), deferring specific details to later sections. Section 3 provides details of the Drucker–Prager model for rate-independent plasticity that defines the constitutive relation (as viscoplasticity is a straight-forward extension of the associated algorithms, detailed in Section 7.2). This is described in terms of the material response at a particular point in the solid, and provides a procedure for evolving stress and plastic strain given a history of total strain. Section 4 applies the results of Section 3, detailing the derivation of the incremental form of the continuum problem of Section 2 and obtaining the governing equation solved within the time-stepping method. In Section 5, we show conditions under which the resulting boundary value problem for the solid satisfies the Drucker stability condition. We also establish conservation of the incremental internal energy in the absence of nontrivial boundary conditions. Section 6 details the spatial discretization, specifically a finite difference method for variable coefficients satisfying a summation-by-parts (SBP) rule with weak enforcement of boundary conditions through the simultaneous-approximation-term (SAT) technique. The combined method will be denoted throughout the paper as SBP-SAT. We show that the semi-discrete problem using the SBP-SAT method mimics the energy balance of the continuum problem. In Section 7, we describe the time stepping method for the overall problem. The solid displacement, stress, and plastic strain are updated in response to time-dependent boundary conditions obtained by updating fault slip in a manner consistent with the friction law. At each time step we solve numerically the incremental equilibrium equation for the solid using an iterative Newton procedure with the return mapping algorithm to calculate stresses consistent with the constitutive theory. The extension of the algorithms to viscoplasticity is also detailed. In Section 8, we present convergence tests and comparisons with numerical solutions from a finite element code to verify our finite difference method. In Section 9 we apply our method to earthquake cycle simulations, and conclude in Section 10 with a discussion.

2. The continuum problem

In this work we assume two-dimensional antiplane shear deformation. The equation for static equilibrium in the medium is given by

$$\frac{\partial \sigma_{xy}}{\partial y} + \frac{\partial \sigma_{xz}}{\partial z} = 0, \quad (y, z) \in [-L_y, L_y] \times [0, L_z], \tag{1}$$

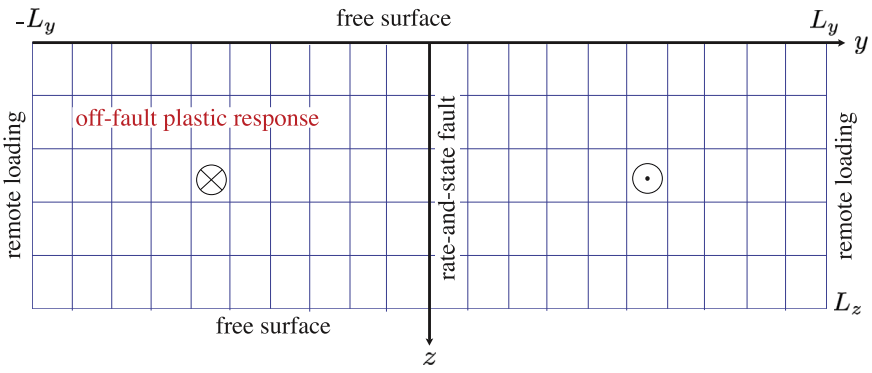

Fig. 1. Schematic diagram for antiplane shear deformation where $u(t, y, z)$ is the out-of-plane displacement. We displace the sides $y = \pm L_y$ at a constant rate, with free surface conditions on the top and bottom. A frictional fault at $y = 0$ is embedded in an elastic–plastic medium.

where σ_{xy} and σ_{xz} are the relevant components of the stress tensor σ. The constitutive relation (Hooke's law) relates stress to elastic strain through the relations

$$\sigma_{xy} = \mu(\gamma_{xy} - \gamma^p_{xy}), \tag{2a}$$

$$\sigma_{xz} = \mu(\gamma_{xz} - \gamma^p_{xz}), \tag{2b}$$

for out-of-plane displacement $u(t, y, z)$, shear modulus μ, total engineering strains

$$\gamma_{xy} = \partial u/\partial y \tag{3a}$$

$$\gamma_{xz} = \partial u/\partial z, \tag{3b}$$

and plastic engineering strains $\gamma^p_{xy}, \gamma^p_{xz}$. Plastic deformation evolves according to a flow rule of the form

$$\dot{\gamma}^p_{xy} = \lambda P_{xy}, \tag{4a}$$

$$\dot{\gamma}^p_{xz} = \lambda P_{xz}, \tag{4b}$$

where λ is the magnitude of the plastic strain rate (a positive, scalar function of the stress), which is nonzero only when plastic deformation occurs. P_{xy}, P_{xz} are dimensionless, (generally nonlinear) functions of the stress, determine how the plastic strain rate is partitioned between different components, and specified by the particular plasticity model (Chen and Han, 1988; Simo and Hughes, 1998). More details are given in Section 3.

A vertical, strike slip fault governed by a rate-and-state friction law lies at the interface $y = 0$ (Dieterich, 1979; Ruina, 1983) (see Fig. 1) where we impose the condition that the jump in displacement is equal to the fault slip, Δu, namely

$$u(t, 0^+, z) - u(t, 0^-, z) = \Delta u(t, z). \tag{5}$$

In addition, we require that the components of the traction vector on the fault be equal and opposite across the interface, which, for antiplane motion, reduces to the second interface condition

$$\sigma_{xy}(t, 0^+, z) = \sigma_{xy}(t, 0^-, z). \tag{6}$$

Slow tectonic loading is imposed by displacing the remote boundaries at a constant relative rate V_p and the top and bottom boundaries are assumed to be free surfaces. We assume the solution u is anti-symmetric across the fault interface (i.e. $u(t, y, z) = -u(t, -y, z)$ for $0 \le y \le L_y$) so that (6) is satisfied by construction, and so we may focus on one side of the fault, namely $(y, z) \in [0, L_y] \times [0, L_z]$ (see Erickson and Dunham, 2014 for details and a discussion on the choice of boundary conditions). For the one-sided problem the boundary conditions are thus given by

$$u(t, 0, z) = \Delta u/2, \tag{7a}$$

$$u(t, L_y, z) = V_p t/2, \tag{7b}$$

$$\sigma_{xz}(t, y, 0) = 0, \tag{7c}$$

$$\sigma_{xz}(t, y, L_z) = 0. \tag{7d}$$

In the rate-and-state friction framework, shear stress on the fault, denoted τ (and related to σ_{xy} as detailed below), is equated with frictional strength through the relation

$$\tau = \sigma_n f(V, \psi), \tag{8}$$

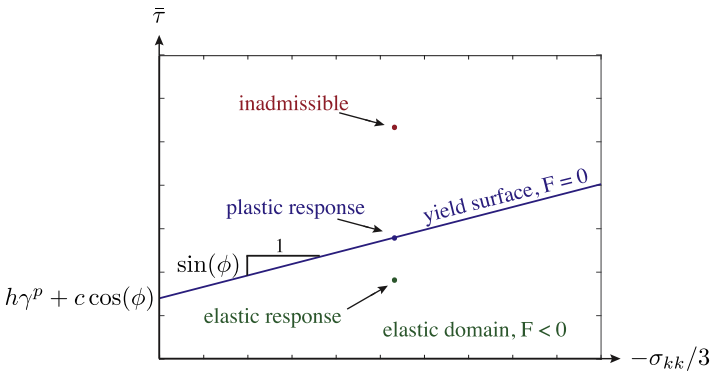

Fig. 2. The Drucker–Prager yield condition for yield function F. Elastic response occurs for states of stress that lie below the yield surface, while plastic response occurs for states on the surface. States above the yield surface are inadmissible. The slope of the line is defined by the angle of internal friction ϕ, while the y-intercept depends further on cohesion c and hardening modulus h. (For interpretation of the references to color in this figure, the reader is referred to the web version of this article.)

where

$$V = \Delta\dot{u} \tag{9}$$

denotes the slip velocity, ψ is an internal state variable, σ_n is the effective normal stress and f is a friction coefficient that takes the particular form

$$f(V,\psi) = a\sinh^{-1}\left(\frac{V}{2V_0}e^{\psi/a}\right) \tag{10}$$

(Dieterich, 1979; Ruina, 1983). We assume the state variable ψ evolves to the aging law form of evolution, namely

$$\frac{d\psi}{dt} = \frac{bV_0}{D_c}\left(e^{(f_0-\psi)/b} - \frac{V}{V_0}\right). \tag{11}$$

With the aging law, state can evolve in the absence of slip, and therefore may be more suitable for modeling the interseismic period. In Eqs. (10) and (11), a and b are dimensionless parameters quantifying the direct effect and state evolution, respectively, f_0 is a reference friction at a reference slip velocity V_0, and D_c is the state evolution distance (Marone, 1998).

In Section 7 we describe how the slip Δu is obtained in a manner consistent with the fault friction law (8), where τ is related to σ_{xy} through the following. Solving the equilibrium Eq. (1) provides the quasistatic stresses σ_{xy}, σ_{xz}. Since disregarding inertia entirely is known to cause slip velocity $V\to\infty$ in finite time (after which no solution exists), we incorporate the radiation damping approximation to inertia (Rice, 1993). Thus τ is defined to be

$$\tau = \sigma_{xy}(t,0,z) - \eta_{rad}V \tag{12}$$

where $-\eta_{rad}V$ is the stress due to radiation damping and $\eta_{rad} = \mu/(2c_s)$ is half the shear-wave impedance (not to be confused with viscosity η for viscoplastic flow) for shear wave speed $c_s = \sqrt{\mu/\rho}$ and material density ρ.

3. Elastoplastic constitutive theory

In this section, we review the Drucker–Prager elastoplastic constitutive theory that is used to evolve stress and plastic strain (in response to an imposed total strain history at a particular material point).

3.1. Drucker–Prager plasticity

Throughout this work we assume infinitesimal strains. Hooke's law (introduced in (2) for the antiplane setting) can be expressed generally by

$$\sigma = C : (\epsilon - \epsilon^p) \tag{13}$$

where ϵ and ϵ^p are the total and plastic strain tensors. The fourth order elasticity tensor C_{ijkl} for an isotropic solid is given by

$$C_{ijkl} = K\delta_{ij}\delta_{kl} + \mu\left(\delta_{ik}\delta_{jl} + \delta_{il}\delta_{jk} - (2/3)\delta_{ij}\delta_{kl}\right), \tag{14}$$

where K is the bulk modulus. Stresses in the medium are constrained by a Drucker–Prager yield condition, see Fig. 2. For rate-independent response with linear, isotropic hardening, the yield function is given by

$$F(\sigma,\gamma^p) = \bar{\tau} - (\sigma_Y + h\gamma^p), \tag{15}$$

where γ^p is the hardening parameter (equivalent plastic strain, defined below) and h is the hardening modulus. In this work we assume $h > 0$ is constant (we say the response is strain-softening if $h < 0$, and perfectly plastic if $h = 0$). The elastic domain in stress space is given by $\mathbb{E}_\sigma = \{(\sigma, \gamma^p) : F(\sigma, \gamma^p) \leq 0\}$ and plastic flow ensues when the yield condition

$$F(\sigma, \gamma^p) = 0 \tag{16}$$

is met. The second invariant of the deviatoric stress is

$$\bar{\tau} = \sqrt{s_{ij} s_{ij}/2} \tag{17}$$

for $s_{ij} = \sigma_{ij} - \sigma_{kk}\delta_{ij}/3$. The yield stress is given by

$$\sigma_Y = -(\sigma_{kk}/3)\sin\phi + c\cos\phi, \tag{18}$$

where c is the cohesion and ϕ is the internal friction angle. Plastic strain evolves according to the flow rule (introduced in Eq. (4)) given by

$$\dot{\epsilon}^p_{ij} = \lambda P_{ij}, \tag{19}$$

where $\lambda = \sqrt{2\dot{e}^p_{ij}\dot{e}^p_{ij}}$ is the deviatoric plastic strain rate for $e^p_{ij} = \epsilon^p_{ij} - \epsilon^p_{kk}\delta_{ij}/3$. Thus

$$\gamma^p(t) = \int_0^t \lambda(s)\, ds, \tag{20}$$

and P_{ij} (specified in the next section) quantifies how plastic strain is distributed between different components of the plastic strain rates. The constitutive theory is closed by including the Kuhn–Tucker loading/unloading (complementarity) conditions

$$\lambda \geq 0, \quad F \leq 0, \quad \lambda F = 0, \tag{21}$$

(which ensure that plastic flow can only occur if stresses lie on the yield surface) and the consistency (persistency) condition

$$\lambda \dot{F} = 0, \tag{22}$$

so that if plastic flow occurs, the stress state must persist on the yield surface for some positive period of time.

3.2. Elastoplastic tangent stiffness tensor

In rate form, Hooke's law (13) expresses stress rate in terms of total strain rate, namely

$$\dot{\sigma}_{ij} = C^{ep}_{ijkl}\dot{\epsilon}_{kl}, \tag{23}$$

where the continuum elastoplastic tangent stiffness tensor $C^{ep}_{ijkl} = C^{ep}_{ijkl}(\sigma)$ is a nonlinear function of stress. We derive this tensor following Simo and Hughes (1998), by first taking the time derivative of the yield function, and then using (19) and the time derivative of (20):

$$\begin{aligned}\dot{F} = \frac{\partial F}{\partial \sigma_{ij}}\dot{\sigma}_{ij} + \frac{\partial F}{\partial \gamma^p}\dot{\gamma}^p &= \frac{\partial F}{\partial \sigma_{ij}} C_{ijkl}(\dot{\epsilon}_{kl} - \dot{\epsilon}^p_{kl}) + \frac{\partial F}{\partial \gamma^p}\dot{\gamma}^p \\ &= \frac{\partial F}{\partial \sigma_{ij}} C_{ijkl}\dot{\epsilon}_{kl} - \lambda\left(\frac{\partial F}{\partial \sigma_{ij}} C_{ijkl} P_{kl} - \frac{\partial F}{\partial \gamma^p}\right).\end{aligned} \tag{24}$$

Assuming that

$$\left(\frac{\partial F}{\partial \sigma_{ij}} C_{ijkl} P_{kl} - \frac{\partial F}{\partial \gamma^p}\right) > 0, \tag{25}$$

(in order to ensure consistency with (21) and (22), see Simo and Hughes, 1998 for more details), we can solve $\dot{F} = 0$ for λ, namely

$$\lambda = \frac{\left\langle \frac{\partial F}{\partial \sigma_{ij}} C_{ijkl}\dot{\epsilon}_{kl} \right\rangle}{\frac{\partial F}{\partial \sigma_{mn}} C_{mnop} P_{op} - \frac{\partial F}{\partial \gamma^p}}, \tag{26}$$

where the brackets denote the ramp function $\langle x \rangle = \frac{x + |x|}{2}$. Taking the time derivative of the stress and substituting in the flow rule yields

$$\dot{\sigma}_{ij} = C_{ijkl}(\dot{\epsilon}_{kl} - \lambda P_{kl}) = C_{ijkl}\left(\dot{\epsilon}_{kl} - \frac{\left\langle \frac{\partial F}{\partial \sigma_{mn}} C_{mnop}\dot{\epsilon}_{op} \right\rangle}{\frac{\partial F}{\partial \sigma_{qr}} C_{qrst} P_{st} - \frac{\partial F}{\partial \gamma^p}} P_{kl}\right), \tag{27}$$

which allows us to express the continuum elastoplastic tangent stiffness tensor

$$C^{ep}_{ijkl} = \begin{cases} C_{ijkl} & \text{if } \lambda = 0, \\ C_{ijkl} - \dfrac{C_{ijop}P_{op}C_{mnkl}\frac{\partial F}{\partial \sigma_{mn}}}{\frac{\partial F}{\partial \sigma_{qr}}C_{qrst}P_{st} - \frac{\partial F}{\partial \gamma^p}} & \text{if } \lambda > 0. \end{cases} \tag{28}$$

Note that C^{ep} is symmetric in the same manner as the elastic tensor given in (14) (namely, that $C^{ep}_{ijkl} = C^{ep}_{jikl} = C^{ep}_{ijlk} = C^{ep}_{klij}$), if the flow rule (19) is associative (i.e. if $P_{ij} = \frac{\partial F}{\partial \sigma_{ij}}$). For Drucker–Prager plasticity,

$$P_{ij} = s_{ij}/(2\bar{\tau}) + (\beta/3)\delta_{ij}, \tag{29}$$

where β determines the degree of plastic dilatancy. Thus the flow rule is associative only if $\beta = \sin(\phi)$.

Expression (28) is thus

$$C^{ep}_{ijkl} = \begin{cases} C_{ijkl} & \text{if } \lambda = 0, \\ C_{ijkl} - \frac{\frac{\mu^2}{\bar{\tau}^2}s_{ij}s_{kl} + \frac{\mu K}{\bar{\tau}}\left[\sin(\phi)s_{ij}\delta_{kl} + \beta\delta_{ij}s_{kl}\right] + \beta K^2\sin(\phi)\delta_{ij}\delta_{kl}}{\mu + \beta K\sin(\phi) + h} & \text{if } \lambda > 0 \end{cases} \tag{30}$$

and associativity (symmetry of C^{ep}_{ijkl}) holds in the general case if $\beta = \sin\phi$.

4. The governing equation in incremental form

Because of the nonlinearity of the constitutive relation (2), a typical approach taken is to consider the rate form, given by (23), and posit the equilibrium Eq. (1) in terms of an infinitesimal displacement increment du (Chen and Han, 1988; Dunne and Petrinic, 2006; Simo and Hughes, 1998). In this section, we derive the incremental equilibrium equation as well as the specific forms of the relevant elastoplastic moduli. Note that although du is an infinitesimally small increment in the continuum setting, it is taken to be finite when the problem is discretized in time as done in Section 7.

In the case of antiplane strain, the only non-zero strains are γ_{xy}, γ_{xz}. For notational purposes, we therefore denote the relevant components of the fourth-order tensor C as $C_{xyxy} = C_{11}, C_{xyxz} = C_{12}, C_{xzxy} = C_{21}$, and $C_{xzxz} = C_{22}$. We use similar notation to denote relevant components of the elastoplastic tangent stiffness tensor, C^{ep}, introduced in the previous section.

Using the rate form (23) allows us to replace (2) with an expression solely in terms of increments of stress $d\sigma$ and strain $d\gamma$, namely

$$d\sigma_{xy} = C^{ep}_{11}d\gamma_{xy} + C^{ep}_{12}d\gamma_{xz}, \tag{31a}$$

$$d\sigma_{xz} = C^{ep}_{21}d\gamma_{xy} + C^{ep}_{22}d\gamma_{xz}, \tag{31b}$$

where

$$d\gamma_{xy} = \frac{\partial du}{\partial y}, \quad d\gamma_{xz} = \frac{\partial du}{\partial z} \tag{32}$$

are the incremental total engineering strains and du is the (infinitesimal) displacement increment.

Relations (31), along with the strain–displacement relations (32) are substituted into the incremental form of the equilibrium Eq. (1) and produce the nonlinear equilibrium equation for du given by

$$\frac{\partial}{\partial y}\left[C^{ep}_{11}\frac{\partial du}{\partial y} + C^{ep}_{12}\frac{\partial du}{\partial z}\right] + \frac{\partial}{\partial z}\left[C^{ep}_{21}\frac{\partial du}{\partial y} + C^{ep}_{22}\frac{\partial du}{\partial z}\right] = 0. \tag{33}$$

Recall that the elastoplastic moduli $C^{ep}_{11}, C^{ep}_{12}, C^{ep}_{21}$ and C^{ep}_{22} in Eq. (33) depend nonlinearly on the stress. Forming the 2×2 matrix

$$\bar{C}^{ep}(\sigma) = \begin{bmatrix} C^{ep}_{11} & C^{ep}_{12} \\ C^{ep}_{21} & C^{ep}_{22} \end{bmatrix} \tag{34}$$

(matrix $\bar{C}$ is formed analogously), we derive conditions in Section 5 such that $\det\bar{C}^{ep} > 0$, as is required for well-posedness.

Specified background stresses in the medium, denoted $\sigma^0_{xx}, \sigma^0_{yy}, \sigma^0_{zz}$ are depth variable (see Section 9), and the initial background shear stresses are given by σ^0_{xy} and σ^0_{xz}. Note that from (30), antiplane deformation can activate changes in normal stresses (for example, $d\sigma_{xx} = C^{ep}_{xxxy}d\gamma_{xy} + C^{ep}_{xxxz}d\gamma_{xz}$) unless the relevant components of the tangent stiffness tensor are zero. This scenario can be avoided with the assumption $\beta = 0$ and $\sigma^0_{xx} = \sigma^0_{yy} = \sigma^0_{zz}$, which we make for the rest of this work.

In this work, we assume isotropic elastic moduli $C_{11} = C_{22} = \mu$, and $C_{12} = C_{21} = 0$.

For antiplane strain the specific components for the elastoplastic stiffness tensor (30) are thus

$$C^{ep}_{11} = \begin{cases} \mu & \text{if } \lambda = 0, \\ \mu - \dfrac{\mu\sigma^2_{xy}/\bar{\tau}^2}{1 + h/\mu} & \text{if } \lambda > 0, \end{cases} \tag{35}$$

$$C_{22}^{ep} = \begin{cases} \mu & \text{if } \lambda = 0, \\ \mu - \dfrac{\mu \sigma_{xz}^2/\bar{\tau}^2}{1 + h/\mu} & \text{if } \lambda > 0, \end{cases} \tag{36}$$

and

$$C_{12}^{ep} = C_{21}^{ep} = \begin{cases} 0 & \text{if } \lambda = 0, \\ -\dfrac{\mu \sigma_{xy}\sigma_{xz}/\bar{\tau}^2}{1 + h/\mu} & \text{if } \lambda > 0. \end{cases} \tag{37}$$

Note that matrix $\bar{C}^{ep}$ is symmetric and in the antiplane setting, Drucker–Prager reduces to von-Mises plasticity. Eq. (17) reduces to

$$\bar{\tau} = \sqrt{\sigma_{xy}^2 + \sigma_{xz}^2} \tag{38}$$

and the corresponding flow rule (19) is given by

$$\dot{\gamma}_{xy}^p = \lambda \frac{\sigma_{xy}}{\bar{\tau}}, \quad \dot{\gamma}_{xz}^p = \lambda \frac{\sigma_{xz}}{\bar{\tau}}. \tag{39}$$

The yield stress (18) reduces to

$$\sigma_Y = -(\sigma_{kk}^0/3)\sin\phi + c\cos\phi. \tag{40}$$

5. Incremental energy balance

We now switch from tensor notation used in previous sections to matrix/vector notation, in order to facilitate comparison with the discrete formulation we derive in the next section. We also assume, for ease of the analysis in the following sections, that the boundary conditions for the incremental problem (33) involve general boundary data dg_L, dg_R, dg_T and dg_B at the left, right, top and bottom boundaries (respectively) namely,

$$du(t, 0, z) = dg_L(t, z), \tag{41a}$$

$$du(t, L_y, z) = dg_R(t, z), \tag{41b}$$

$$C_{21}^{ep}\frac{\partial du}{\partial y} + C_{22}^{ep}\frac{\partial du}{\partial z}\bigg|_{z=0} = dg_T(t, y), \tag{41c}$$

$$C_{21}^{ep}\frac{\partial du}{\partial y} + C_{22}^{ep}\frac{\partial du}{\partial z}\bigg|_{z=L_z} = dg_B(t, y). \tag{41d}$$

Later, however, we outline how we specify incremental boundary conditions so as to impose fault slip, slow tectonic loading and free surface conditions, as expressed in (7).

Assuming the solution to (33) with boundary conditions (41) is sufficiently smooth, we multiply (33) by the incremental velocity $d\dot{u}$ and integrate by parts, yielding the following energy balance

$$\frac{d}{dt}dE = \int_0^{L_z} d\dot{u}\, d\sigma_{xy}\Big|_0^{L_y} dz + \int_0^{L_y} d\dot{u}\, d\sigma_{xz}\Big|_0^{L_z} dy, \tag{42}$$

where the incremental internal energy is defined by

$$dE = \frac{1}{2}\int_0^{L_y}\int_0^{L_z} dU^T \bar{C}^{ep}(\sigma)\, dU dy dz \tag{43}$$

for vector

$$dU = \begin{bmatrix} \partial du/\partial y \\ \partial du/\partial z \end{bmatrix}.$$

The symmetric 2×2 matrix $\bar{C}^{ep}$ has eigenvalues

$$\lambda_1, \lambda_2 = \begin{cases} \mu & \text{if } \lambda = 0, \\ \mu,\ h/(1 + h/\mu) & \text{if } \lambda > 0 \end{cases} \tag{44}$$

and (25) implies that $1 + h/\mu > 0$. $\bar{C}^{ep}$ is therefore positive definite for rate-independent plasticity if and only if $h > 0$ (Horn and Johnson, 1985). If $h < 0$, $\det(\bar{C}^{ep}) = \lambda_1\lambda_2 \le 0$, which results in a loss of ellipticity of the equilibrium Eq. (33) and a loss of solvability. This case violates Drucker's first stability postulate (requiring $dU^T\bar{C}^{ep}(\sigma)\, dU > 0$) and can lead to problems including loss of uniqueness of the solution (Bower, 2010; Drucker, 1959; Jain, 2008). For the case $h \le 0$, the constitutive theory therefore requires modification (through the introduction of rate dependence, for example). Thus for rate-independent

plasticity, $h>0$ is required; however, viscosity in the viscoplastic model ensures a positive definite matrix, even if $h=0$ (see Section 7.2).

Note that in terms of increments, the rate of change of the internal energy can be decomposed into the sum of the rate of change of the mechanical (elastic strain) energy and the plastic dissipation (a positive quantity), namely,

$$\frac{d}{dt}dE = \frac{d}{dt}\int_0^{L_y}\int_0^{L_z}\frac{1}{2}[dU^e]^T\bar{C}\,dU^e\,dy\,dz + \int_0^{L_y}\int_0^{L_z}[dU^e]^T\bar{C}\,d\dot{U}^p\,dy\,dz, \tag{45}$$

where $dU^e = dU - dU^p$, is the vector of elastic strains and the plastic strain vector is

$$dU^p = \begin{bmatrix} d\gamma_{xy}^p \\ d\gamma_{xz}^p \end{bmatrix}.$$

For simplicity in the analysis only (see Erickson and Dunham, 2014 for details), we may take the boundary data $dg_L = dg_R = dg_T = dg_B = 0$ and show that (42) reduces to

$$\frac{d}{dt}dE = 0, \tag{46}$$

showing conservation of the incremental internal energy (or dissipation of the incremental mechanical energy) in the absence of source terms and nontrivial boundary conditions (i.e., in the absence of work done by body forces or surface tractions).

6. The spatial discretization

The nonlinearities present in the governing Eq. (33) with boundary conditions (41) make analytical solutions difficult, if not impossible to obtain, except perhaps in certain limiting cases. SBP-SAT finite difference methods are often used, however, to obtain numerical approximations to solutions of nonlinear problems (e.g., Navier–Stokes from fluid mechanics (Nordström et al., 2007), although the stability analysis can be challenging and is generally approached by consideration of the linearized or "frozen coefficient" problem. If the solution is sufficiently smooth (which is not guaranteed for our problem), the linearized analysis is often enough to ensure convergence for the nonlinear problem (Gustafsson, 2008).

We discretize Eq. (33) using the second-order accurate, narrow-stencil, summation-by-parts (SBP) finite difference operators for second derivatives, originally defined in Mattsson and Nordström (2004) for constant coefficients, and for variable coefficients in Mattsson (2011). Time-dependent boundary conditions are imposed and the elastoplastic moduli $C_{11}^{ep}, C_{12}^{ep}, C_{21}^{ep}$ and C_{22}^{ep} are nonlinear functions of the current stress state (or equivalently, of the displacement increment). We use a Newton's method with line search to solve the nonlinear equation, detailed in Section 7.3. At each time step, and each iteration of Newton's method we consider the moduli as frozen, spatially variable coefficients, and use the static counterpart of the spatial discretization of the anisotropic acoustic wave equation in heterogeneous media (Virta and Mattsson, 2014).

We apply second-order accurate SBP operators and introduce the 2D operators by first considering one spatial dimension. The 1D domain $y\in[0,\,L]$ is discretized into N_y+1 grid points $y_0, y_1, \ldots, y_{N_y}$ with grid spacing $\Delta y = L/N_y$. First derivatives are approximated by $\frac{\partial u}{\partial y} \approx \mathbf{Du}$, where $\mathbf{u} = [u_0,\ u_1,\ \ldots\ u_{N_y}]^T$ is the grid function and matrix $\mathbf{D} = \mathbf{H^{-1}Q}$ is an $N_y+1\times N_y+1$ finite difference operator. $\mathbf{H}$ and $\mathbf{Q}$ are also $N_y+1\times N_y+1$ matrices and the building blocks for the SBP operators. $\mathbf{H}$ is a diagonal, positive definite quadrature matrix defining a discrete norm on the space of grid functions

$$||\mathbf{u}||_H^2 = \mathbf{u}^T H\mathbf{u}, \tag{47}$$

and $\mathbf{Q}$ is an almost skew-symmetric matrix such that $\mathbf{Q}+\mathbf{Q}^T = \mathrm{diag}[-1,0,0,\ldots,0,1]$. The SBP operators are derived such that they mimic integration-by-parts and provide a discrete energy estimate (that mimics its continuum counterpart). Namely, the relation $\int_0^L u\frac{\partial u}{\partial y}dy = \frac{1}{2}\left[u^2(L)-u^2(0)\right]$ is obtained by integration-by-parts and is mimicked discretely by $\mathbf{u}^T\mathbf{H}(\mathbf{Du}) = \frac{1}{2}\mathbf{u}(\mathbf{Q}+\mathbf{Q}^T)\mathbf{u} = \frac{1}{2}(u_N^2-u_0^2)$. If $p(y)$ defines the variable coefficient, the narrow-stencil second derivative operator for variable coefficients is given by

$$\frac{\partial}{\partial y}\left(p(y)\frac{\partial}{\partial y}\right) \approx \mathbf{D_2^p} = \mathbf{H}^{-1}(-\mathbf{M}^p + \mathbf{pBS}), \tag{48}$$

where $\mathbf{B} = \mathrm{diag}[-1,\ldots,1]$, and $\mathbf{S}$ approximates the first derivative operator on the boundary. Matrix $\mathbf{M}^p = \mathbf{D}^T\mathbf{HpD} + \mathbf{R}^p$, where $\mathbf{R}^p = \frac{(\Delta y)^3}{4}(\mathbf{D_2})^T\mathbf{C_2pD_2}$ (correcting the typographical error in Eq. (21) in Erickson and Dunham, 2014) is a positive definite damping matrix and $\mathbf{C}_2 = \mathrm{diag}[0,1,1,\ldots,1,1,0]$ (Mattsson, 2011). Matrix $\mathbf{p} = \mathrm{diag}[p(y_0),\ \ p(y_1),\ \ \ldots\ \ p(y_{N_y})]$ is a $N_y+1\times N_y+1$ coefficient matrix (all coefficient matrices are denoted similarly, with bold notation).

In 2D, we discretize the domain $[0,\,L_y]\times[0,\,L_z]$ with an $N_y+1\times N_z+1$-point grid, defined by

$$y_i = i\Delta y, \quad i=0,1,\ldots,N_y, \quad \Delta y = L_y/N_y, \tag{49a}$$

$$z_i = i\Delta z, \quad i=0,1,\ldots,N_z, \quad \Delta z = L_z/N_z, \tag{49b}$$

where Δy and Δz are the grid spacings in each direction. Thus $u_{i,j} \approx u(y_j, z_i)$. Letting $N = (N_y + 1)(N_z + 1)$, the $N \times 1$ grid vector $\mathbf{u}$ in 2D is given by

$$\mathbf{u} = [\mathbf{u}_0^T, \quad \mathbf{u}_1^T, \quad \dots \quad \mathbf{u}_{N_y}^T] \tag{50}$$

where

$$\mathbf{u}_i = [u_{0,i}, \quad u_{1,i}, \quad \dots \quad u_{N_z,i}], \text{ for } i = 0, \dots N_y. \tag{51}$$

The 2D variable coefficient $p(y, z)$ defined on $[0, L_y] \times [0, L_z]$ is transformed to the $N \times N$ diagonal matrix $\mathbf{p} = \text{diag}[\mathbf{p}_0^T, \mathbf{p}_1^T, \dots, \mathbf{p}_{N_y}^T]$ using analogous notation. To form the SBP finite difference operators in 2D we make use of the Kronecker product. Recall that if matrix $\mathbf{A}$ is size $p \times q$ and $\mathbf{B}$ is $r \times s$ then the Kronecker product of the two is of size $pr \times qs$ and given by

$$\mathbf{A} \otimes \mathbf{B} = \begin{bmatrix} a_{0,0}\mathbf{B} & \cdots & a_{0,N}\mathbf{B} \\ \vdots & & \vdots \\ a_{N,0}\mathbf{B} & \cdots & a_{N,N}\mathbf{B} \end{bmatrix}. \tag{52}$$

In addition, the following identities hold:

$$(\mathbf{A} \otimes \mathbf{B})(\mathbf{C} \otimes \mathbf{D}) = (\mathbf{AC}) \otimes (\mathbf{BD}), \tag{53a}$$

$$(\mathbf{A} \otimes \mathbf{B})^{-1} = (\mathbf{A}^{-1} \otimes \mathbf{B}^{-1}) \text{ if } \mathbf{A} \text{ and } \mathbf{B} \text{ are invertible}, \tag{53b}$$

$$(\mathbf{A} \otimes \mathbf{B})^T = \mathbf{A}^T \otimes \mathbf{B}^T. \tag{53c}$$

We can thus extend any 1D operator $\mathbf{P}$ to 2D (in the y and z direction, respectively) by

$$\mathbf{P}_y = (\mathbf{P} \otimes \mathbf{I}), \tag{54a}$$

$$\mathbf{P}_z = (\mathbf{I} \otimes \mathbf{P}). \tag{54b}$$

The first and second derivative operators in 2D are thus

$$\frac{\partial}{\partial y} \approx \mathbf{D}_y, \tag{55a}$$

$$\frac{\partial}{\partial z} \approx \mathbf{D}_z, \tag{55b}$$

$$\frac{\partial}{\partial y}\left(p(y,z)\frac{\partial}{\partial y}\right) \approx \mathbf{D}_{2y}^{\mathbf{p}} = \mathbf{H}_y^{-1}\left[-\mathbf{D}_y^T \mathbf{p} \mathbf{H}_y \mathbf{D}_y - \mathbf{R}_y^p + \mathbf{p}\mathbf{B}_y \mathbf{S}_y\right], \tag{55c}$$

$$\frac{\partial}{\partial z}\left(p(y,z)\frac{\partial}{\partial z}\right) \approx \mathbf{D}_{2z}^{\mathbf{p}} = \mathbf{H}_z^{-1}\left[-\mathbf{D}_z^T \mathbf{p} \mathbf{H}_z \mathbf{D}_z - \mathbf{R}_z^p + \mathbf{p}\mathbf{B}_z \mathbf{S}_z\right], \tag{55d}$$

where $\mathbf{R}_y^p, \mathbf{R}_z^p$ are positive definite damping matrices in 2D (see Erickson and Dunham, 2014 for details). The equilibrium Eq. (33), along with boundary conditions (41), is thus discretized by

$$\mathbf{D}_{2y}^{\mathbf{C}_{11}^{ep}}\mathbf{du} + \mathbf{D}_y \mathbf{C}_{12}^{ep} \mathbf{D}_z \mathbf{du} + \mathbf{D}_z \mathbf{C}_{21}^{ep} \mathbf{D}_y \mathbf{du} + \mathbf{D}_{2z}^{\mathbf{C}_{22}^{ep}}\mathbf{du} + \mathbf{P}_L + \mathbf{P}_R + \mathbf{P}_T + \mathbf{P}_B = \mathbf{0}, \tag{56}$$

where $\mathbf{du}$ is the incremental displacement grid vector, and the SAT penalty vectors are given by

$$\mathbf{P}_L = \mathbf{H}_y^{-1}(\boldsymbol{\alpha}_L + \beta \mathbf{H}_z^{-1}(-\mathbf{C}_{11}^{ep}\mathbf{S}_y - \mathbf{C}_{12}^{ep}\mathbf{D}_z)^T)\mathbf{H}_z \mathbf{E}_0(\mathbf{du}_L - \mathbf{dg}_L) \tag{57a}$$

$$\mathbf{P}_R = \mathbf{H}_y^{-1}(\boldsymbol{\alpha}_R + \beta \mathbf{H}_z^{-1}(\mathbf{C}_{11}^{ep}\mathbf{S}_y + \mathbf{C}_{12}^{ep}\mathbf{D}_z)^T)\mathbf{H}_z \mathbf{E}_N(\mathbf{du}_R - \mathbf{dg}_R) \tag{57b}$$

$$\mathbf{P}_T = -\mathbf{H}_z^{-1}(\mathbf{I}_y \otimes \mathbf{E}_0)(\left[-\mathbf{C}_{22}^{ep}\mathbf{S}_z\mathbf{du} - \mathbf{C}_{21}^{ep}\mathbf{D}_y\mathbf{du}\right]_T - \mathbf{dg}_T) \tag{57c}$$

$$\mathbf{P}_B = -\mathbf{H}_z^{-1}(\mathbf{I}_y \otimes \mathbf{E}_N)(\left[\mathbf{C}_{22}^{ep}\mathbf{S}_z\mathbf{du} + \mathbf{C}_{21}^{ep}\mathbf{D}_y\mathbf{du}\right]_B - \mathbf{dg}_B). \tag{57d}$$

Recall that the coefficient matrices in (56) depend nonlinearly on the stress $\boldsymbol{\sigma}$. The notation $\mathbf{du}_L$ is the restriction of the grid vector $\mathbf{du}$ to the left boundary and $\mathbf{du}_R$, $\mathbf{du}_T$, $\mathbf{du}_B$, are the restrictions to the right, top and bottom boundaries (respectively). Vector $\mathbf{dg}_L$ is the boundary data dg_L evaluated at the grid and $\mathbf{dg}_R$, $\mathbf{dg}_T$, $\mathbf{dg}_B$ are defined analogously. Matrices $\mathbf{E}_0$ and $\mathbf{E}_N$ map the restricted vectors to full-length ($N \times 1$ length) vectors (see Erickson and Dunham, 2014 for details). Virta and Mattsson (2014) derive conditions on the penalty parameter β and penalty matrices $\boldsymbol{\alpha}_L$, and $\boldsymbol{\alpha}_R$ such that a

semi-discrete energy estimate can be obtained. Following their analysis, the semi-discrete incremental internal energy $\mathbf{dE}$ (a slightly modified analog of (43)) is defined

$$\mathbf{dE} = \frac{1}{2}\mathbf{dU}^T(\mathbf{H}_y \otimes \mathbf{H}_z)\bar{\mathbf{C}}^{ep}\mathbf{dU} + \frac{1}{2}\mathbf{du}^T(\mathbf{R}_y^{\mathbf{C}_{11}^{ep}} \otimes \mathbf{H}_z)\mathbf{du} + \frac{1}{2}\mathbf{du}^T(\mathbf{H}_y \otimes \mathbf{R}_z^{\mathbf{C}_{22}^{ep}})\mathbf{du} + U_1 + U_2. \tag{58}$$

In (58), vector $\mathbf{dU} = [\mathbf{D}_y\mathbf{du}\ \mathbf{D}_z\mathbf{du}]^T$, the positive-definiteness of the $2N \times 2N$, block diagonal matrix

$$\bar{\mathbf{C}}^{ep} = \begin{bmatrix} \mathbf{C}_{\mathbf{11}}^{\mathbf{ep}} & \mathbf{C}_{12}^{ep} \\ \mathbf{C}_{21}^{ep} & \mathbf{C}_{22}^{ep} \end{bmatrix} \tag{59}$$

follows from that of $\bar{C}^{ep}$, and U_1, U_2 are positive quantities, see Appendix A. Assuming zero-boundary data, as in the continuum problem, the semi-discrete equations are shown to satisfy the energy estimate

$$\frac{d}{dt}\mathbf{dE} \leq 0, \tag{60}$$

which ensures stability of the method, see Appendix A for more details. Note that for our application problems in Section 9 we desire better resolution near the fault and free surface, and therefore consider a non-uniform grid spacing. In Appendix A we detail the stability analysis for a grid with non-uniform spacing; the uniform grid spacing assumed in this section (to maintain flow of the discussion) is a special case.

7. Time stepping

In this section, we explain the time stepping method for the overall problem. This is done by first updating slip and the state variable along the frictional fault. The update to slip, along with the remaining boundary conditions, generates an increment of load. Updates to the displacement, stresses and plastic strains (that occur in the volume in response to the load) are then computed.

We introduce a time discretization so that notationally, superscripts on a particular field imply we are considering a *finite* increment over a discrete time step. We assume the system is equilibrated at time t^n with stresses consistent with the constitutive theory of Section 3. Slip and state variable along the fault are updated via a Runge–Kutta method with adaptive time stepping (see Section 7.4 for details). These updates provide the incremental boundary data $\mathbf{dg}_L^{n+1}$ along the fault, which, together with $\mathbf{dg}_R^{n+1}, \mathbf{dg}_T^{n+1}, \mathbf{dg}_B^{n+1}$, correspond to an increment of load applied over the time step $dt = t^{n+1} - t^n$ that drives the system to a new state. In what follows, we describe the latter part update, namely, how the displacement increment and the associated stresses and plastic strains are updated in response to the load in a manner that accounts for plastic response.

Let the discrete equilibrium Eqs. (56) and (57) be denoted $\mathcal{E}(\mathbf{d\sigma}) = \mathbf{b}$ where vector $\mathbf{b}$ stores the incremental boundary data. At t^{n+1} we wish to obtain both stress and displacement increments that satisfy

$$\mathcal{E}(\mathbf{d\sigma}^{n+1}) = \mathbf{b}^{n+1} \tag{61}$$

and are consistent with the constitutive theory of Section 3, where $\mathbf{d\sigma}^{n+1}$ is related to the displacement increment $\mathbf{du}^{n+1}$ through a discrete form of constitutive relation (31) (which we define shortly) and the discretized strain–displacement relations (32).

To obtain the displacement, stresses and strains at time t^{n+1} we first apply a backward-Euler discretization to the flow rule (19) and equivalent plastic strain

$$\boldsymbol{\gamma}_{xy}^{p,n+1} = \boldsymbol{\gamma}_{xy}^{p,n} + \mathbf{d\lambda}^{n+1}\frac{\boldsymbol{\sigma}_{xy}^{n+1}}{\bar{\boldsymbol{\tau}}^{n+1}} \tag{62a}$$

$$\boldsymbol{\gamma}_{xz}^{p,n+1} = \boldsymbol{\gamma}_{xz}^{p,n} + \mathbf{d\lambda}^{n+1}\frac{\boldsymbol{\sigma}_{xz}^{n+1}}{\bar{\boldsymbol{\tau}}^{n+1}}, \tag{62b}$$

$$\boldsymbol{\gamma}^{p,n+1} = \boldsymbol{\gamma}^{p,n} + \mathbf{d\lambda}^{n+1}, \tag{62c}$$

where $\mathbf{d\lambda}^{n+1} = \boldsymbol{\lambda}^{n+1}dt$. A direct linearization of this discretization implies an associated discrete, incremental form of the constitutive relation given by

$$\mathbf{d}\sigma_{ij}^{n+1} = \mathcal{C}_{ijkl}^{ep}(\boldsymbol{\sigma}^{n+1})\boldsymbol{d\epsilon}_{kl}^{n+1} \tag{63}$$

where $\mathcal{C}^{ep}$ is the *consistent* tangent stiffness tensor (and a function of the stress at the end of the time step), derived in the next section. The fully discrete equilibrium equation can thus be expressed

$$\mathcal{E}(\mathcal{C}^{ep}(\boldsymbol{\sigma}^{n+1})\mathbf{du}^{n+1}) = \mathbf{b}^{n+1}, \tag{64}$$

and is a nonlinear function of $\mathbf{du}^{n+1}$.

To solve (64) we proceed via a Newton-type method which utilizes the partial derivative

$$\frac{\partial\mathcal{E}}{\partial\mathbf{du}^{n+1}} = \frac{\partial\mathcal{E}}{\partial\mathbf{d}\sigma_{ij}^{n+1}}\mathcal{C}_{ijkl}^{ep}(\boldsymbol{\sigma}^{n+1})\frac{\partial\mathbf{d}\epsilon_{kl}^{n+1}}{\partial\mathbf{du}^{n+1}} \tag{65}$$

and incorporates the consistent tangent stiffness tensor. We set iteration index $k=0$ and compute an initial, elastic guess $\mathbf{du}^{n+1,(k)}$ to the displacement increment, obtained by assuming $\mathcal{C}^{ep}=\mathbf{C}$ and solving (64). Consistent stresses $\boldsymbol{\sigma}^{n+1,(k)}$ associated with $\mathbf{du}^{n+1,(k)}$ are obtained from the *return mapping algorithm* which is based on the backward Euler discretization (62), and detailed in the next section. Deferring specific details until Section 7.4, if the new, consistent stress state satisfies equilibrium, then the final fields are those at iteration k, and the process is considered done.

If equilibrium is not satisfied, however, the displacement increment $\mathbf{du}^{n+1,(k)}$ must be adjusted (and thus adjustments to the stress and plastic strains must be made). The displacement increment is updated by solving (64) via an iterative Newton-type method that solves the *linearized* equilibrium problem

$$\mathcal{E}(\mathcal{C}^{ep}(\boldsymbol{\sigma}^{n+1,(k)})\mathbf{du}^{n+1,(k+1)})=\mathbf{b}^{n+1}. \tag{66}$$

and the return mapping algorithm provides associated consistent stresses $\boldsymbol{\sigma}^{n}+1,(k+1)$ (Simo and Hughes, 1998; de Souza Neto et al., 2008). This iterative procedure continues until equilibrium has been satisfied with an appropriate convergence criterion met (see Section 7.3). The displacement $\mathbf{u}^{n+1}=\mathbf{u}^{n}+\mathbf{du}^{n+1}$ can then be formed from the converged value of the finite increment $\mathbf{du}^{n+1}$.

7.1. The return mapping algorithm

Within the Newton iteration described in the previous section, the finite displacement increment $\mathbf{du}^{n+1,(k)}$ is obtained and stresses consistent with the plastic constitutive theory must be updated (Simo and Hughes, 1998). In this section, we describe how to obtain $\boldsymbol{\sigma}^{n+1,(k)}$. First, the strains associated with $\mathbf{du}^{n+1,(k)}$ are computed

$$\boldsymbol{\gamma}_{xy}^{n+1,(k)}=\boldsymbol{\gamma}_{xy}^{n}+\mathbf{d}\boldsymbol{\gamma}_{xy}^{n+1,(k)}, \tag{67a}$$

$$\boldsymbol{\gamma}_{xz}^{n+1,(k)}=\boldsymbol{\gamma}_{xz}^{n}+\mathbf{d}\boldsymbol{\gamma}_{xz}^{n+1,(k)}, \tag{67b}$$

and allow us to compute the elastic trial state (denoted with asterisk *)

$$\boldsymbol{\gamma}^{*,p,n+1,(k)}=\boldsymbol{\gamma}^{p,n}, \tag{68a}$$

$$\boldsymbol{\sigma}_{xz}^{*,n+1,(k)}=\mu(\boldsymbol{\gamma}_{xz}^{n+1,(k)}-\boldsymbol{\gamma}_{xz}^{p,n})=\boldsymbol{\sigma}_{xz}^{n}+\mu\mathbf{d}\boldsymbol{\gamma}_{xz}^{n+1,(k)}, \tag{68b}$$

$$\boldsymbol{\sigma}_{xy}^{*,n+1,(k)}=\mu(\boldsymbol{\gamma}_{xy}^{n+1,(k)}-\boldsymbol{\gamma}_{xy}^{p,n})=\boldsymbol{\sigma}_{xy}^{n}+\mu\mathbf{d}\boldsymbol{\gamma}_{xy}^{n+1,(k)}, \tag{68c}$$

assuming no additional plastic strain has accrued over the time step.

The final stress state at time t^{n+1} must satisfy $F\leq 0$, where the yield function is defined in (15) for yield stress (40). If the elastic trial stresses satisfy $F\leq 0$, then they are accepted as the final stresses. If the trial stresses lie outside the yield surface ($F>0$), however, they are be "mapped back" onto the yield surface by adjusting the plastic strains so that $F(\boldsymbol{\sigma}^{n+1},(k),\boldsymbol{\gamma}^{p,n+1,(k)})=0$ is satisfied (Simo and Hughes, 1998).

Substituting Eqs. (62a), (62b) into (68b), (68c) yields

$$\boldsymbol{\sigma}_{xy}^{*,n+1}=\boldsymbol{\sigma}_{xy}^{n+1}(1+\mu\mathbf{d}\boldsymbol{\lambda}^{n+1}/\bar{\boldsymbol{\tau}}^{n+1}) \tag{69a}$$

$$\boldsymbol{\sigma}_{xz}^{*,n+1}=\boldsymbol{\sigma}_{xz}^{n+1}(1+\mu\mathbf{d}\boldsymbol{\lambda}^{n+1}/\bar{\boldsymbol{\tau}}^{n+1}). \tag{69b}$$

From (69) we calculate

$$\begin{aligned}\bar{\boldsymbol{\tau}}^{*,n+1}&=\sqrt{(\boldsymbol{\sigma}_{xy}^{*,n+1})^2+(\boldsymbol{\sigma}_{xz}^{*,n+1})^2}\\&=\bar{\boldsymbol{\tau}}^{n+1}+\mu\mathbf{d}\boldsymbol{\lambda}^{n+1}.\end{aligned} \tag{70}$$

Re-arranging (70), noting that $F(\boldsymbol{\sigma}^{n+1},\boldsymbol{\gamma}^{p,n+1})=0$, and substituting in (62c) yields the plastic consistency condition

$$\mathbf{d}\boldsymbol{\lambda}^{n+1}=F(\boldsymbol{\sigma}^{*,n+1},\boldsymbol{\gamma}^{*,p,n+1})/(h+\mu), \tag{71}$$

where $\boldsymbol{\gamma}^{*,p,n+1}$ is given by (68c). Finally, solving (69) for $\boldsymbol{\sigma}_{xy}^{n+1}$ and $\boldsymbol{\sigma}_{xz}^{n+1}$ yields

$$\boldsymbol{\sigma}_{xy}^{n+1,(k)}=\frac{\boldsymbol{\sigma}_{xy}^{*,n+1,(k)}}{1+\mu\mathbf{d}\boldsymbol{\lambda}^{n+1,(k)}/\bar{\boldsymbol{\tau}}^{n+1}}=\frac{\boldsymbol{\sigma}_{xy}^{*,n+1,(k)}(\bar{\boldsymbol{\tau}}^{*,n+1,(k)}-\mu\mathbf{d}\boldsymbol{\lambda}^{n+1,(k)})}{\bar{\boldsymbol{\tau}}^{*,n+1,(k)}} \tag{72a}$$

$$\boldsymbol{\sigma}_{xz}^{n+1,(k)}=\frac{\boldsymbol{\sigma}_{xz}^{*,n+1,(k)}}{1+\mu\mathbf{d}\boldsymbol{\lambda}^{n+1,(k)}/\bar{\boldsymbol{\tau}}^{n+1,(k)}}=\frac{\boldsymbol{\sigma}_{xz}^{*,n+1,(k)}(\bar{\boldsymbol{\tau}}^{*,n+1,(k)}-\mu\mathbf{d}\boldsymbol{\lambda}^{n+1},(k))}{\bar{\boldsymbol{\tau}}^{*,n+1,(k)}}, \tag{72b}$$

which expresses the final stress state entirely in terms of the computed elastic trial stresses.

The consistent elastoplastic tangent stiffness tensor $\mathcal{C}^{ep}_{ijkl}$ in (64) is obtained by a linearization of the return-mapping algorithm. We derive these consistent moduli in Appendix B, with specific components (ommitting superscripts $n+1$) given by (bold face notation is not used as these moduli are derived independently of a spatial discretization)

$$\mathcal{C}^{ep}_{11} = \begin{cases} \mu & \text{if } \lambda = 0, \\ \mu - \dfrac{\mu\sigma_{xy}^2/\bar{\tau}^2}{1+h/\mu} - \dfrac{d\lambda\mu^2}{\bar{\tau}}\left[1 - \left(\dfrac{\sigma_{xy}}{\bar{\tau}}\right)^2\right] & \text{if } \lambda > 0, \end{cases} \tag{73}$$

$$\mathcal{C}^{ep}_{22} = \begin{cases} \mu & \text{if } \lambda = 0, \\ \mu - \dfrac{\mu\sigma_{xz}^2/\bar{\tau}^2}{1+h/\mu} - \dfrac{d\lambda\mu^2}{\bar{\tau}}\left[1 - \left(\dfrac{\sigma_{xz}}{\bar{\tau}}\right)^2\right] & \text{if } \lambda > 0, \end{cases} \tag{74}$$

and

$$\mathcal{C}^{ep}_{12} = \mathcal{C}^{ep}_{21} = \begin{cases} 0 & \text{if } \lambda = 0, \\ -\dfrac{\mu\sigma_{xy}\sigma_{xz}/\bar{\tau}^2}{1+h/\mu} - \dfrac{d\lambda\mu^2}{\bar{\tau}}\left[1 - \dfrac{\sigma_{xy}\sigma_{xz}}{\bar{\tau}^2}\right] & \text{if } \lambda > 0, \end{cases} \tag{75}$$

which agree with the continuum moduli in the limit that $d\lambda \to 0$.

It has been shown for many problems that using the consistent tangent moduli (73)–(75) with discretization (64) (to compute numerical solutions to (33)) then the quadratic convergence rate typical of Newton-type iterative methods is achieved. This rate of convergence is often lost, however, if the continuum tangent moduli (35)–(37) are used instead (Simo and Taylor, 1985). In our application problems we thus use the consistent elastoplastic moduli and leave the comparison of Newton convergence results to future work.

7.2. Extension to viscoplasticity

Classical Perzyna viscoplasticity (Perzyna, 1966; 1971) is obtained from rate-independent plasticity by replacing the yield condition (16) with $F(\boldsymbol{\sigma}, \boldsymbol{\gamma}^p) = \eta\boldsymbol{\lambda}$, where $\eta > 0$ is the viscosity. A viscoplastic response alters the return mapping algorithm in the previous section through the following: if the computed elastic trial stresses are such that $F(\boldsymbol{\sigma}^{*,n+1}, \boldsymbol{\gamma}^{*,p,n+1}) > 0$, then Eqs. (70) and (71) are replaced with

$$\bar{\boldsymbol{\tau}}^{*,n+1} = \bar{\boldsymbol{\tau}}^{n+1} + \mu\frac{F^{n+1}}{\eta}dt \tag{76}$$

and

$$\mathbf{d}\boldsymbol{\lambda}^{n+1} = F(\boldsymbol{\sigma}^{*,n+1}, \boldsymbol{\gamma}^{*,p,n+1})/(\eta/dt + h + \mu). \tag{77}$$

The consistent elastoplastic tangent moduli (73)–(75) can also be derived from linearizing the return-mapping algorithm (see Appendix B), yielding

$$\mathcal{C}^{ep}_{11} = \begin{cases} \mu & \text{if } \boldsymbol{\lambda} = 0, \\ \mu - \dfrac{\mu\sigma_{xy}^2/\bar{\tau}^2}{\dfrac{\eta/\mu}{dt} + 1 + h/\mu} - \dfrac{d\lambda\mu^2}{\bar{\tau}}\left[1 - \left(\dfrac{\sigma_{xy}}{\bar{\tau}}\right)^2\right] & \text{if } \boldsymbol{\lambda} > 0, \end{cases} \tag{78}$$

$$\mathcal{C}^{ep}_{22} = \begin{cases} \mu & \text{if } \lambda = 0, \\ \mu - \dfrac{\mu\sigma_{xz}^2/\bar{\tau}^2}{\dfrac{\eta/\mu}{dt} + 1 + h/\mu} - \dfrac{d\lambda\mu^2}{\bar{\tau}}\left[1 - \left(\dfrac{\sigma_{xz}}{\bar{\tau}}\right)^2\right] & \text{if } \lambda > 0, \end{cases} \tag{79}$$

and

$$\mathcal{C}^{ep}_{12} = \mathcal{C}^{ep}_{21} = \begin{cases} 0 & \text{if } \lambda = 0, \\ -\dfrac{\mu\sigma_{xy}\sigma_{xz}/\bar{\tau}^2}{\dfrac{\eta/\mu}{dt} + 1 + h/\mu} - \dfrac{d\lambda\mu^2}{\bar{\tau}}\left[1 - \dfrac{\sigma_{xy}\sigma_{xz}}{\bar{\tau}^2}\right] & \text{if } \lambda > 0. \end{cases} \tag{80}$$

Note that for a fixed η, if $dt \to 0$, the consistent elastoplastic moduli (78)–(80) approach the elastic moduli. Furthermore, for $\eta > 0$, we can take $h = 0$ and still guarantee that $\bar{\mathcal{C}}^{ep}$ is positive definite.

7.3. Newton iteration with return-mapping

We let $k=0$, $\mathbf{du}^{n+1,(k)}$ be the initial (elastic) guess for the displacement increment $\mathbf{du}^{n+1}$, and iterate as follows.

Step 1: Compute the strain increments

$$\mathbf{d}\boldsymbol{\gamma}_{xy}^{n+1,(k)} = \mathbf{D}_y \mathbf{du}^{n+1,(k)}, \tag{81a}$$

$$\mathbf{d}\boldsymbol{\gamma}_{xz}^{n+1,(k)} = \mathbf{D}_z \mathbf{du}^{n+1,(k)}. \tag{81b}$$

Step 2: Compute the elastic trial state and use the return mapping algorithm to obtain the consistent stresses $\boldsymbol{\sigma}_{xy}^{n+1,(k)}, \boldsymbol{\sigma}_{xz}^{n+1,(k)}$ and plastic strain $\boldsymbol{\gamma}^{p,n+1,(k)}$.

Step 3: Check if equilibrium is sufficiently satisfied. That is, check if a stopping criterion is met, for example, $||\mathcal{E}(\mathcal{C}^{ep}(\boldsymbol{\sigma}^{n+1,(k)})\mathbf{du}^{n+1,(k)}) - \mathbf{b}^{n+1}|| < tol)$, where tol is a specified tolerance. If so, set $\mathbf{u}^{n+1} = \mathbf{u}^n + \mathbf{du}^{n+1,(k)}$, the remaining fields are those at iteration (k), and the Newton iteration is complete. Otherwise set $k = k+1$, solve $\mathcal{E}(\mathcal{C}^{ep}(\boldsymbol{\sigma}^{n+1,(k)})\mathbf{du}^{n+1,(k+1)}) = \mathbf{b}^{n+1}$ for $\mathbf{du}^{n+1,(k+1)}$ and return to step 1, iterating until the Newton method converges and equilibrium is met.

7.4. Time stepping method

In this section we provide details of time stepping for the overall problem, which includes details of the update to slip and the state variable along the fault, and provides an initial guess for the off-fault fields. As stated in Section 2, rate-and-state friction, as used in our algorithm, provides the set of differential Eqs. (9)–(11) that are used to evolve the fault boundary displacement (i.e., fault slip). We modify the method from Erickson and Dunham (2014) in order to incorporate off-fault plasticity. Bold-face type is again used to denote spatially discrete quantities. We assume the body is equilibrated (with consistent stresses) at time t^n and that $\mathbf{V}^n$ and $\boldsymbol{\psi}^n$ are known. The following time-stepping method is illustrated in the context of a forward Euler step, but we use Matlab's adaptive, fourth order Runge–Kutta method with a relative tolerance of 10^{-7}.

Step 1. Update slip and state on the fault by explicitly integrating

$$\boldsymbol{\Delta}\mathbf{u}^{n+1} = \boldsymbol{\Delta}\mathbf{u}^n + dt\mathbf{V}^n \tag{82a}$$

$$\boldsymbol{\psi}^{n+1} = \boldsymbol{\psi}^n + dtG(\mathbf{V}^n, \boldsymbol{\psi}^n). \tag{82b}$$

Step 2. Set the boundary data in (41):

$$\mathbf{dg}_L^{n+1} = dt\mathbf{V}^n/2,$$

$$\mathbf{dg}_R^{n+1} = dtV_p/2,$$

$$\mathbf{dg}_T^{n+1} = \mathbf{dg}_B^{n+1} = 0,$$

form $\mathbf{b}^{n+1}$ and solve for an elastic increment $\mathbf{du}^{n+1,(0)}$; i.e., take $\mathcal{C}^{ep} = \mathbf{C}$ and solve the discrete Eq. (64).

Step 3. Correct the initial elastic guess $\mathbf{du}^{n+1,(0)}$ by iterating following the Newton procedure in Section 7.3 until convergence is reached, thus obtaining $\mathbf{u}^{n+1}, \boldsymbol{\sigma}_{xy}^{n+1}, \boldsymbol{\sigma}_{xz}^{n+1}, \boldsymbol{\gamma}_{xy}^{p,n+1}, \boldsymbol{\gamma}_{xz}^{p,n+1}, \boldsymbol{\gamma}^{p,n+1}$.

Step 4. Compute the shear stress $\boldsymbol{\tau}_{qs}^{n+1} = \boldsymbol{\sigma}_{xy}^{n+1}|_{y=0}$ on the fault.

Step 5. Equate shear stress with frictional strength $\boldsymbol{\tau}_{qs}^{n+1} - \eta_{rad}\mathbf{V}^{n+1} = \boldsymbol{\sigma}_n f(\mathbf{V}^{n+1}, \boldsymbol{\psi}^{n+1})$ and solve for the updated slip velocity $\mathbf{V}^{n+1}$ (solved using a local, safe-guarded Newton method) and return to step 1.

8. Convergence tests and comparison with finite element solution

We conduct two studies to verify our numerical method. The first study is a convergence test of our spatial discretization and time-stepping for an elastic problem; the second study is a comparison test with a finite element solution for the same plasticity model.

For the first study we proceed with the method of manufactured solutions and show that our numerical solution is converging to the exact solution at the correct rate (Roache, 1998). The nonlinearity introduced by plasticity makes this procedure difficult, thus we solve the anisotropic elastic version by assuming that the elastoplastic moduli do not vary with stress or time, but rather in space only. We want to check that our incremental procedure will provide a numerical approximation to the exact solution to the non-incremental equilibrium equation

$$\frac{\partial}{\partial y}\left[C_{11}^{ep}(y,z)\frac{\partial u}{\partial y} + C_{12}^{ep}(y,z)\frac{\partial u}{\partial z}\right] + \frac{\partial}{\partial z}\left[C_{21}^{ep}(y,z)\frac{\partial u}{\partial y} + C_{22}^{ep}(y,z)\frac{\partial u}{\partial z}\right] = 0, \tag{83}$$

where the moduli in (83) are known functions of space. Let the exact displacement (denoted with a hat) to (83) be that given in Erickson and Dunham (2014), namely

$$\hat{u}(t,y,z) = \frac{\delta}{2}K(t)\Phi(y,z) + \frac{V_p t}{2}[1-\Phi(y,z)] + \frac{\tau^\infty}{\mu}y, \tag{84}$$

which provides the exact (elastic) stresses (also denoted with hats)

$$\hat{\sigma}_{xy} = C_{11}^{ep}(y,z)\partial\hat{u}/\partial y + C_{12}^{ep}(y,z)\partial\hat{u}/\partial z \tag{85a}$$

$$\hat{\sigma}_{xz} = C_{21}^{ep}(y,z)\partial\hat{u}/\partial y + C_{22}^{ep}(y,z)\partial\hat{u}/\partial z. \tag{85b}$$

Appropriate source terms are added to (83) so that $\hat{u}$ is indeed the solution. In the construction of the exact solution (84), $K(t)$ controls the time-dependency of the solution, δ is the total slip that occurs during the event, τ^{∞} is a parameter that defines the remote stress, and Φ describes the spatial dependency of the solution. The specific forms are given by

$$\delta = V_p\bar{t} + V_{\min}\bar{t}, \tag{86a}$$

$$K(t) = \frac{1}{\pi}\left[\tan^{-1}\left(\frac{t-\bar{t}}{t_w}\right) + \frac{\pi}{2}\right] + \frac{V_{\min}}{\delta}, \tag{86b}$$

$$\Phi(y,z) = \frac{H(H+y)}{(H+y)^2+z^2}, \tag{86c}$$

where $\bar{t}$ denotes the event time, t_w denotes the time scale over which the event occurs, $V_{\min}$ defines a minimum slip velocity throughout the simulation, and H defines a locking depth. For the elastic moduli, we assume the following forms

$$C_{11}^{ep} = \mu - \frac{\mu c_1(y,z)^2/|c|^2}{1+h/\mu}, \tag{87a}$$

$$C_{22}^{ep} = \mu - \frac{\mu c_2(y,z)^2/|c|^2}{1+h/\mu}, \tag{87b}$$

$$C_{12}^{ep} = C_{21}^{ep} = -\frac{\mu c_1(y,z)c_2(y,z)/|c|^2}{1+h/\mu}, \tag{87c}$$

where

$$c_1(y,z) = \frac{H_1^2}{H_1^2+z^2}\frac{L_1^2}{L_1^2+y^2}, \tag{88a}$$

$$c_2(y,z) = \frac{H_2^2}{H_2^2+z^2}\frac{L_2^2}{L_2^2+y^2} \tag{88b}$$

and $|c|^2 = c_1^2 + c_2^2$. Thus the moduli form a symmetric, positive definite matrix $\bar{C}^{ep}$ if $h > 0$. The exact slip along the fault is

$$\Delta\hat{u}(t,z) = 2\hat{u}(t,0,z) = \delta K(t)\Phi(0,z) + V_p t[1-\Phi(0,z)], \tag{89}$$

with slip velocity

$$\hat{V}(t,z) = \frac{\partial u^*}{\partial t}|_{y=0^+} - \frac{\partial u^*}{\partial t}|_{y=0^-} = \delta K'(t)\Phi(y,z) + V_p[1-\Phi(0,z)]. \tag{90}$$

Lastly, since $\hat{\tau}(t,z) = \hat{\sigma}_{xy}(t,0,z)$, we can solve (8) for the exact state variable

$$\hat{\psi} = a\ln\left[\frac{2V_0}{\hat{V}}\sinh\left(\frac{\hat{\tau}-\eta_{rad}\hat{V}}{\sigma_n a}\right)\right] \tag{91}$$

which implies that a source term must also be added to state evolution

$$\dot{\psi} = G(V,\psi) + s(t,z) \tag{92}$$

where

$$s = \dot{\hat{\psi}} - G(\hat{V},\hat{\psi}). \tag{93}$$

All parameter values used in the convergence tests are given in Table 1. At the end of the simulation ($t_f = 70$ years), we compute the relative error between the exact and the numerical approximation in both the discrete H-norm and the energy-norm, defined by

$$\text{Error}_H(h) = ||\mathbf{u}-\hat{\mathbf{u}}||_H/||\hat{\mathbf{u}}||_H \tag{94a}$$

$$\text{Error}_E(h) = ||\mathbf{u}-\hat{\mathbf{u}}||_E/||\hat{\mathbf{u}}||_E \tag{94b}$$

where

$$||\mathbf{u}||_H^2 = \sum_{i=1}^{M}||\mathbf{du}_i||_H^2 \tag{95a}$$

Table 1
Parameters used in the manufactured solution convergence tests.

Parameter	Definition	Value
L_z	Fault length	24 km
L_y	Off-fault domain length	24 km
ℓ_Z	z-length scale for coordinate transform	5 km
ℓ_Y	y-length scale for coordinate transform	5 km
H	Locking depth	14 km
L_1	y-Length scale for c_1	5 km
H_1	z-Length scale for c_1	6 km
L_2	y-Length scale for c_2	4 km
H_2	z-Length scale for c_2	5 km
ρ	Density	2670 kg/m^3
μ	Shear modulus	30 GPa
h	Hardening modulus	30 GPa
σ_n	Normal stress on fault	50 MPa
τ^∞	Remote shear stress	40 MPa
t_f	Final simulation time	70 years
$\bar{t}$	Event nucleation time	35 years
t_w	Timescale for event duration	10 s
a	Rate-and-state parameter	0.015
b	Rate-and-state parameter	0.02
D_c	Critical slip distance	0.4 m
V_p	Plate rate	10^{-9} m/s
V_0	Reference velocity	10^{-6} m/s
f_0	Reference friction coefficient	0.6

Table 2
Relative error in the discrete **H**- and energy-norms with $N = N_y = N_z$. The rate of convergence approaches 2, as expected for a method with second-order accuracy.

N	$\text{Error}_H(h)$	Rate	$\text{Error}_E(h)$	Rate
2^4	1.030×10^{-3}	–	1.236×10^{-3}	–
2^5	2.867×10^{-4}	1.845	3.514×10^{-4}	1.814
2^6	7.433×10^{-5}	1.947	9.242×10^{-5}	1.927
2^7	1.883×10^{-5}	1.981	2.360×10^{-5}	1.970
2^8	4.741×10^{-6}	1.990	5.967×10^{-6}	1.984

$$||\mathbf{u}||_E^2 = \sum_{i=1}^{M} \mathbf{dE}_i \tag{95b}$$

where $||\mathbf{du}||_H^2 = (\mathbf{du})^T (\mathbf{H}_y \otimes \mathbf{H}_z)(\mathbf{du})$, M is the number of adaptive, Runge–Kutta time steps and $\mathbf{dE}$ is the incremental internal energy defined by (58). Table 2 shows that we are achieving second-order convergence, as expected.

Because this first verification study confirmed convergence for an anisotropic elastic problem, the purpose of the next study is to validate our results with plasticity. For the second validation study, we compare results of the solution to a boundary value problem subject to Drucker–Prager plasticity. Results from our finite difference code are compared to those from a finite element solution using the OpenSees Software Framework (Mazzoni et al., 2009) and available at http://opensees.berkeley.edu.

We want to confirm that our incremental approach using Eq. (33) (in the context of the time stepping method outlined in the previous section) solves the non-incremental form of the governing Eq. (1), on the domain $(y, z) \in [0, L] \times [0, L]$ with boundary conditions given by

$$u(0, z) = 0 \tag{96a}$$

$$u(L, z) = g(z) \tag{96b}$$

$$\sigma_{xz}(y, 0) = 0 \tag{96c}$$

$$\sigma_{xz}(y, L) = 0. \tag{96d}$$

Boundary data $g(z)$ and all parameter values are listed in Table 3. Stresses are subject to the Drucker–Prager yield condition (15) with constant yield stress σ_Y. We assume an equal grid spacing $\Delta = \Delta y = \Delta z$ of both 1 km ($N_y = N_z = 24$) and 200 m ($N_y = N_z = 120$). Fig. 3 shows solutions from the finite difference solution to the plastic boundary value problem with $\Delta = 200$ m, along with the elastic counterpart of the same boundary value problem, in order to illustrate the differences between the two material models. Fig. 3(a)–(c) shows the displacement and two relevant stress components of the plastic

Table 3
Parameters used in antiplane plastic case for comparision of FDM and FEM.

Parameter	Definition	Value
L_z	Fault length	24 km
L_y	Off-fault domain length	24 km
μ	Shear modulus	32.038 GPa
ρ	Material density	2670 kg/m^3
$g(z)$	Right boundary condition	$-\cos(\pi z/12)+1$ (m)
σ_Y	Yield stress	4 MPa
ϕ	Angle of internal friction	0
h	Hardening modulus	32.038 GPa

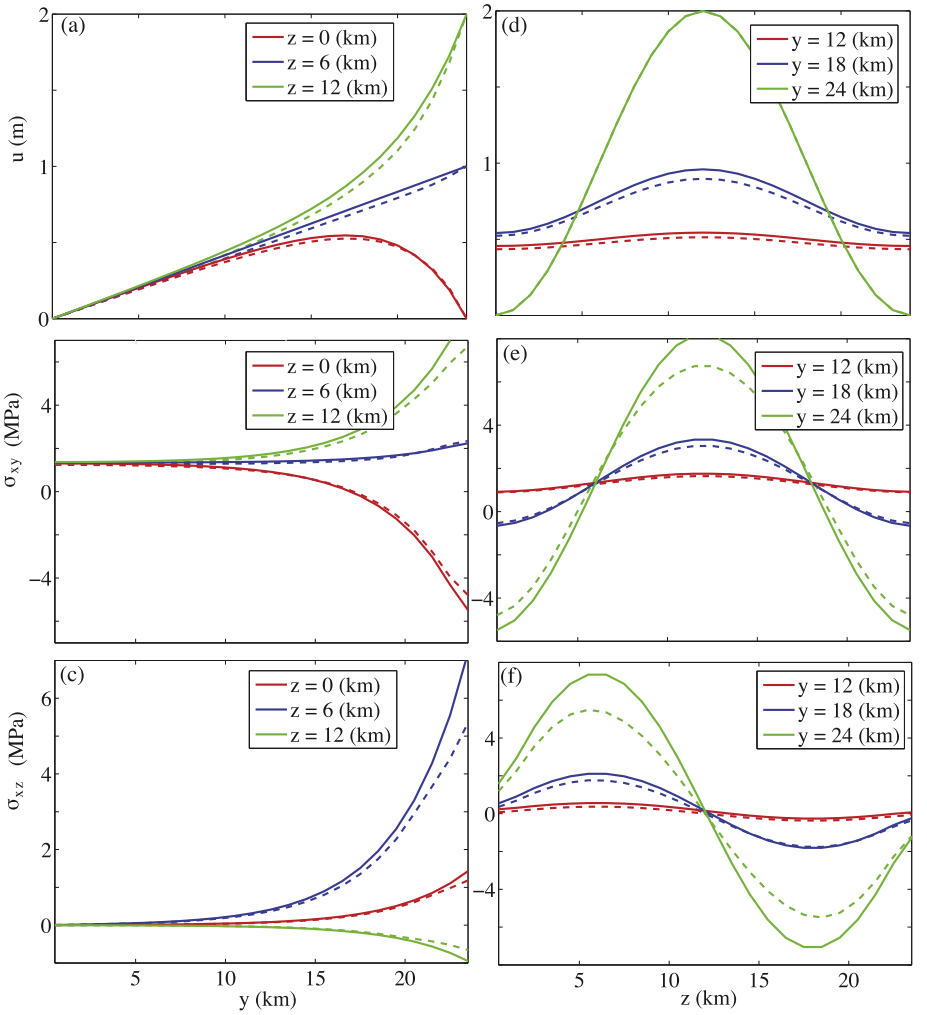

Fig. 3. Contours of solution to (1) with boundary conditions (96) for elastic (solid lines) and plastic (dashed lines) material response. (a) and (b) displacement and (c)–(f) stress components. Plastic effects are seen most prominently in the stress contours which are reduced due to the yield condition.

solution (in dashed lines) and the elastic solution (solid lines) at different z-values. Fig. 3(d)–(f) are the equivalent fields at various y-values. Although plasticity mildly affects the displacement field, the stresses are significantly reduced in amplitude, particularly near $y = 24$ km. Fig. 4 compares contours from the finite difference and finite element solution with $\Delta = 1$ km. The finite difference solution is plotted in solid colors, while the finite element solution is plotted with black circles. The displacement fields in Fig. 4(a) and (b) are quite similar, but error is visible in the computed stresses, particularly in Fig. 4(d) near $y = 24$ km. This error is visibly decreased when mesh refining, as shown in Fig. 5. Absolute and relative errors between the computed fields using the two methods are denoted by $\text{err}_u^a = ||\mathbf{u}^{FD} - \mathbf{u}^{FE}||_2$ and $\text{err}_u^r = ||\mathbf{u}^{FD} - \mathbf{u}^{FE}||_2/||\mathbf{u}^{FE}||_2$, respec-

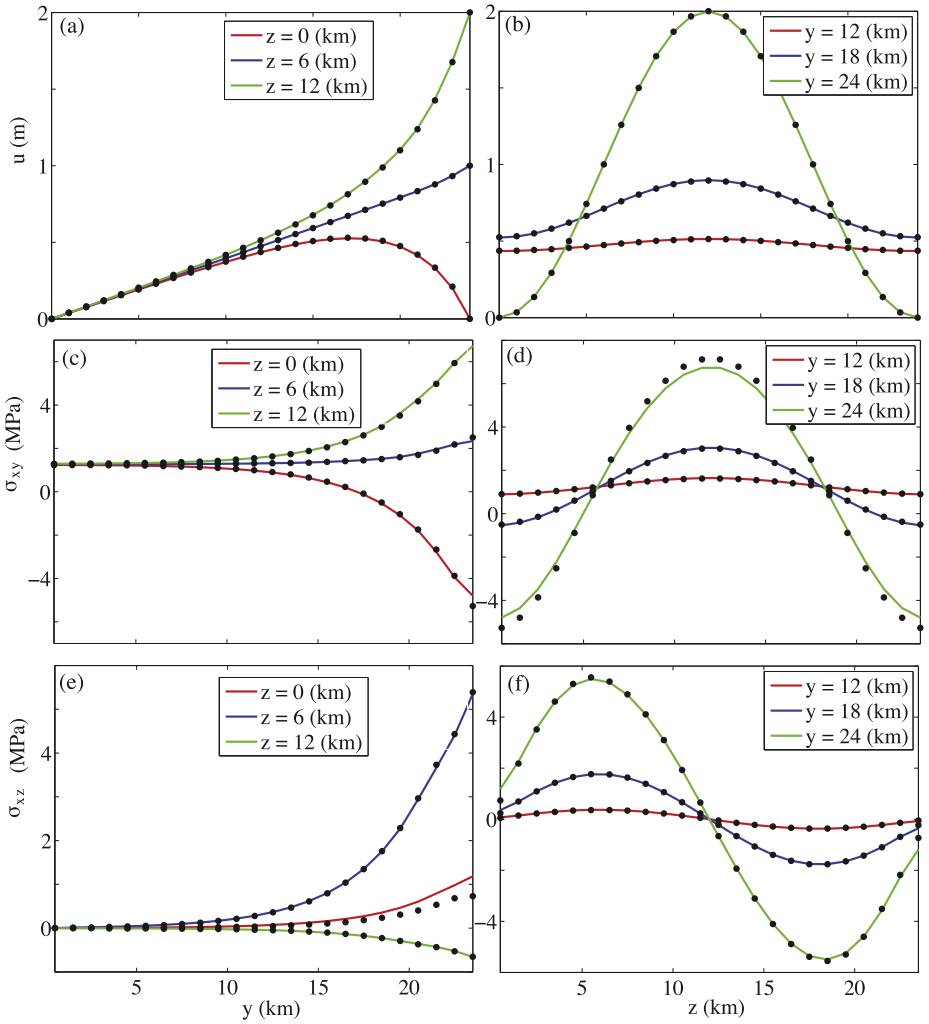

Fig. 4. Contours of solution to (1) with boundary conditions (96) for plastic material response using the finite difference method (solid lines) and the finite element solution (black dots). (a) and (b) displacement and (c)–(f) stress components, with $N_y = N_z = 24$ points.

Table 4
Absolute and relative error between our finite difference solution and that obtained from the finite element code in the discrete L^2-norm for $N_y = N_z = 24, 120$.

N	err^a_u	err^r_u	$\text{err}^a_{\sigma_{xy}}$	$\text{err}^r_{\sigma_{xy}}$	$\text{err}^a_{\sigma_{xx}}$	$\text{err}^r_{\sigma_{xz}}$
24	1.06×10^{0}	3.27×10^{-2}	1.72×10^{0}	3.72×10^{-2}	4.76×10^{-2}	3.22×10^{-2}
120	9.87×10^{-2}	3.04×10^{-3}	1.92×10^{-1}	4.14×10^{-3}	3.81×10^{-3}	2.70×10^{-4}

tively, and errors for other fields are defined analogously. Results shown in Table 4 suggest the two methods produce similar results.

9. Application

We are interested in how changes in viscosity, isotropic hardening and cohesion affect features of the earthquake cycle. We find that all three parameters influence the magnitude and off-fault extent of plastic strain, and that in all cases, plasticity affects the amount of slip on the fault in the shallow sub-surface during each rupture. We use the combined spatial discretization and time-stepping method detailed in previous sections to simulate multiple earthquake cycles with off-fault plasticity. The fault is governed by rate-and-state friction with depth-variable parameters a and b (see Fig. 6(a)). Where $a - b < 0$ defines the velocity-weakening (seismogenic) zone, below which the fault creeps interseismically. As an initial study, we assume that the effective normal stresses in the medium are given by $\sigma^0_{xx} = \sigma^0_{yy} = \sigma^0_{zz} = -(\rho - \rho_w)gz + P_{atm}$ where ρ_w is the density of water, g is the acceleration due to gravity and atmospheric pressure P_{atm} is set to 0.1 MPa. The

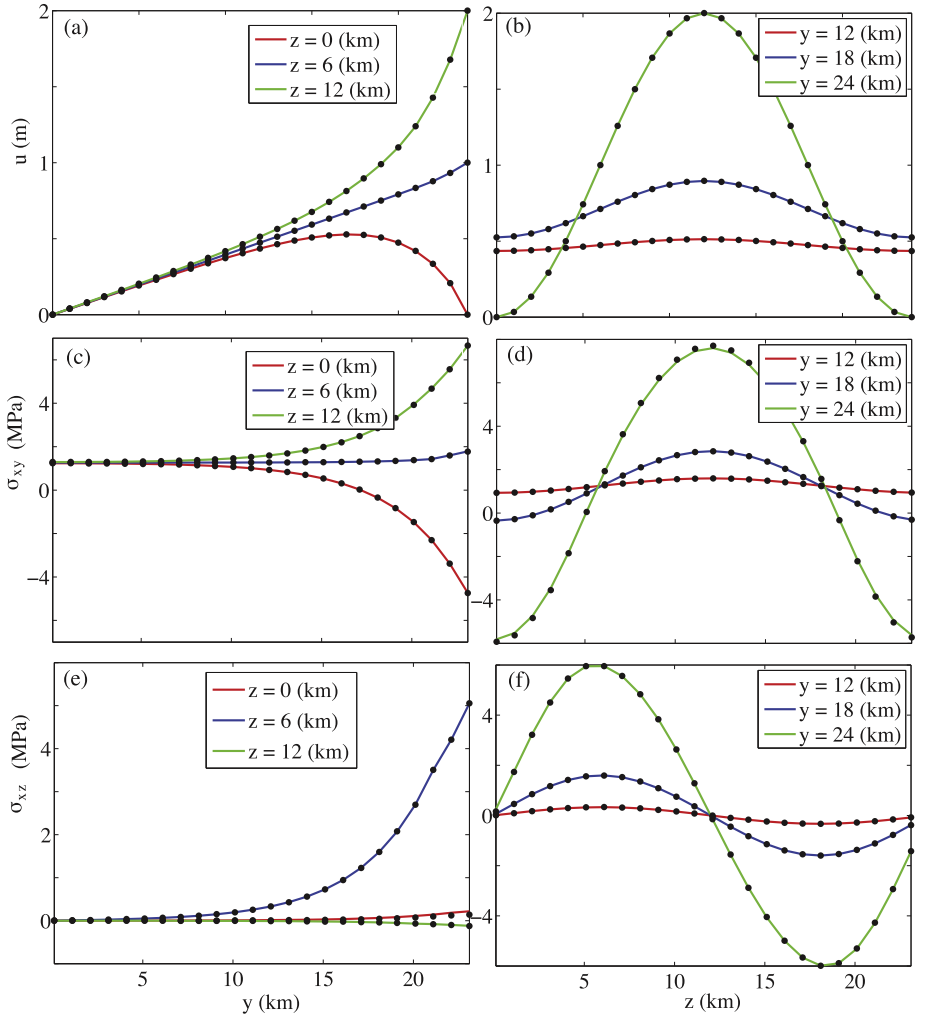

Fig. 5. Contours of solution to (1) with boundary conditions (96) for plastic material response using the finite difference method (solid lines) and the finite element solution (black dots). (a) and (b) displacement and (c)–(f) stress components, with $N_y = N_z = 120$ points.

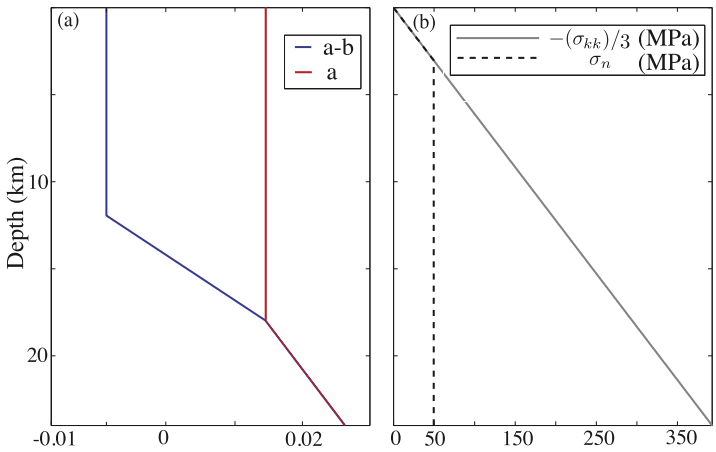

Fig. 6. (a) Frictional parameters $a - b$ vary with depth. (b) Normal stress σ_n on fault vs. normal stresses in medium.

Table 5
Parameters used in application simulations.

Parameter	Definition	Value
L_z	Fault length	24 km
L_y	Off-fault domain length	24 km
μ	Shear modulus	36 GPa
ρ	Density	2800 kg/m^3
c_s	Shear wave speed	3.586 km/s
ρ_w	Density of water	1000 kg/m^3
σ_n	Normal stress on fault	Depth-variable
τ^∞	Remote shear stress	10^{-7} MPa
a	Rate-and-state parameter	Depth-variable
b	Rate-and-state parameter	Depth-variable
D_c	Critical slip distance	8 mm
V_p	Plate rate	10^{-9} m/s
V_0	Reference velocity	10^{-6} m/s
f_0	Reference friction coefficient	0.6
c	Cohesion	Variable
h	Hardening modulus	Variable
ϕ	Internal friction angle	arctan(0.6)

yield stress (15) is thus linearly increasing with depth, see Fig. 6(b). We assume the pore-pressure in the fault is higher than in the surrounding rock so that although the effective stresses off the fault are depth-variable, effective normal stress on the fault is constant below some depth, see Fig. 6(b) (Rice, 1992). Fixing the internal friction parameter ϕ sets the slope of the yield stress and the yield stress at Earth's surface can be increased or decreased by changing the value of the cohesion c, which we assume is constant with depth. We vary cohesion between 40 and 50 MPa, which are reasonable depth-averaged values of those derived from Hoek–Brown parameters for many rock strength models (Roten et al., 2016). The parameters we use in our simulations are given in Table 5.

To determine grid spacing for our application simulations, Ranjith (2008) found that for antiplane sliding between two anisotropic elastic materials, instability occurs for wave numbers below the critical wave number

$$k_{cr} = \frac{2(b-a)\sigma_n}{D_c\,\mu^*}, \tag{97}$$

where

$$\mu^* = \sqrt{\det(\bar{C}^{ep})}. \tag{98}$$

Thus the length scale

$$h^* = \frac{2\pi}{k_{cr}} = \frac{\pi D_c \mu^*}{(b-a)\sigma_n} \tag{99}$$

must be resolved by the grid to ensure accuracy of the solution.

As in Erickson and Dunham (2014), we also need to resolve the region of rapid strength degradation immediately behind the tip of a propagating rupture, which is typically much smaller than h^*, and involves the rate-and-state parameters a and b in a different manner. By analogy to the corresponding elastic problem (Ampuero and Rubin, 2008), we anticipate that this length scale will be approximately

$$L_b = \frac{\mu^* D_c}{b\,\sigma_n}. \tag{100}$$

For all of our simulations, events nucleate near the transition zone from velocity weakening to velocity strengthening (at a depth of approximately 10 km) and we chose values for parameters η and h primarily for computational (grid resolution) purposes. Since we use a variable grid spacing, we resolve h^* and L_b in our simulations with at least 60 and 5 grid points (respectively) near the free surface, with fewer (down to 12 and 1 grid point, respectively) at the nucleation depth, which we note seems less than desirable. To test that this grid spacing is adequate, however, we double the number of grid points for one scenario and the results appear qualitatively similar, see Appendix C. For the viscoplastic simulations we resolve the viscous relaxation time scale η/μ with at least 5 time steps.

For some parameter regimes, plastic yielding during the interseismic period is possible. For example, a decrease in cohesion c decreases the size of the elastic domain, so that plastic yielding can occur at lower stress states, see Fig. 2. Although in reality plastic yielding may occur during all phases of the earthquake cycle, we chose to explore scenarios where plastic response is limited to the coseismic phase. This choice was made because viscoplasticity introduces the time scale η/h which must be resolved by the time-stepping method. For small values of η/h, the effective response during rupture is plastic. Unfortunately, small η/h cannot be resolved during the interseismic phase without taking unreasonably small time steps, thus we considered large values of c such that plastic response occurs only at those stress levels attained during rupture. The study of plastic yielding during all phases of the earthquake cycle are deferred to future work.

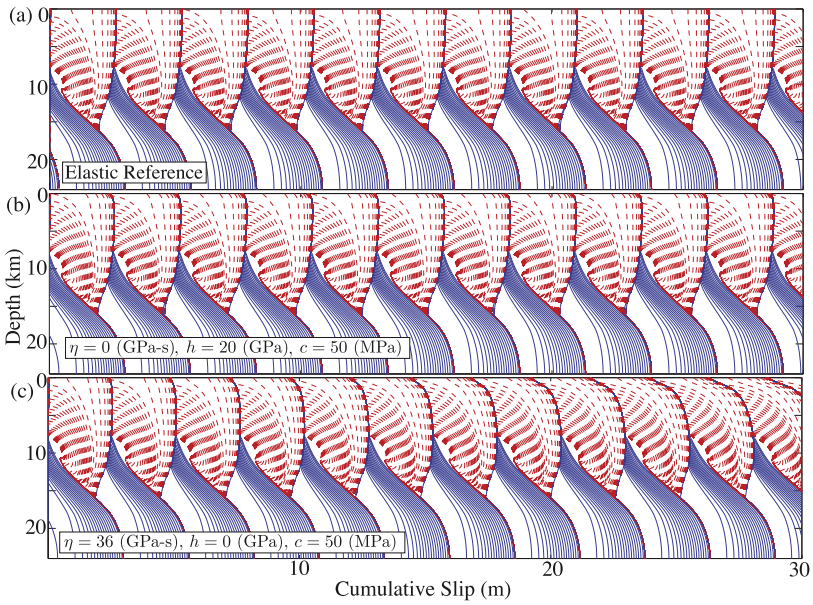

Fig. 7. Snapshots of cumulative slip profiles plotted at 5-a intervals during interseismic period when $\max(V) \leq 1$ mm/s and dashed red profiles plotted at 1 s intervals during quasi-dynamic rupture for (a) elastic reference case, (b) $\eta = 0$ GPa s, $h = 20$ GPa, $c = 50$ MPa, and (c) $\eta = 36$ GPa s, $h = 0$ GPa, $c = 50$ MPa. (For interpretation of the references to color in this figure legend, the reader is referred to the web version of this article.)

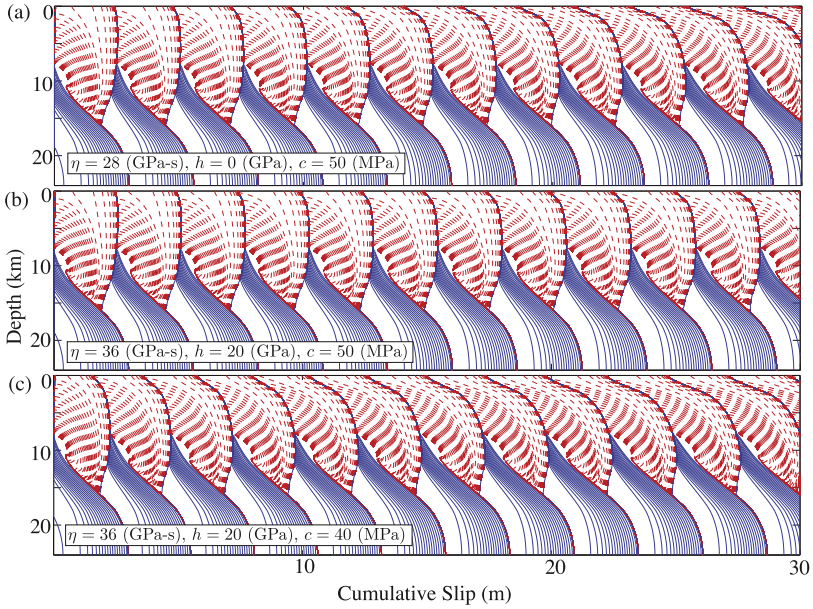

Fig. 8. Snapshots of cumulative slip profiles plotted at 5-a intervals during interseismic period when $\max(V) \leq 1$ mm/s and dashed red profiles plotted at 1 s intervals during quasi-dynamic rupture for (a) $\eta = 28$ GPa s, $h = 0$ GPa, $c = 50$ MPa, (b) $\eta = 36$ GPa s, $h = 20$ GPa, $c = 50$ MPa, and (c) $\eta = 36$ GPa s, $h = 20$ GPa, $c = 40$ MPa. (For interpretation of the references to color in this figure legend, the reader is referred to the web version of this article.)

Figs. 7 and 8 show cumulative slip profiles plotted at 5-a intervals during the interseismic period, which we define to be when $\max(V) \leq 1$ mm/s, and in dashed red contours every 1 s during quasi-dynamic rupture. Fig. 7(a) is the elastic reference case used in Erickson and Dunham (2014), where periodic cycles emerge. Slip below the velocity-weakening region creeps interseismically and approximately 3 m of slip occurs at the surface during each event. Note that during each event, the upper section of the fault catches up with slip at depth, characteristic of an elastic material response. For the plastic simulations, in all cases we found that after the first rupture, slip in the shallow surface is less than the slip at depth. The evolution of this slip deficit with each subsequent event is dictated by the plasticity model, however.

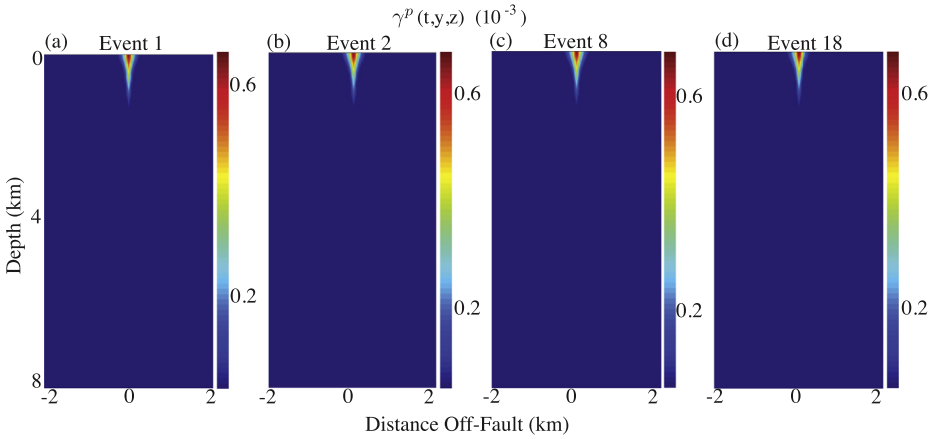

Fig. 9. Off-fault equivalent plastic strain for $\eta = 0$ GPa s, $h = 20$ GPa, $c = 50$ MPa after the first, second, eight and eighteenth rupture events. The magnitude and off-fault extent (~ 100 m during first rupture only) of plastic strain effectively saturates after the first event.

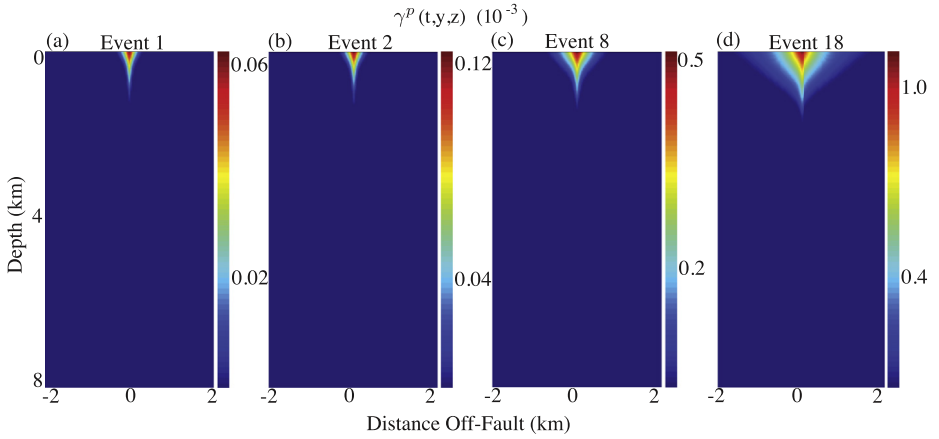

Fig. 10. Off-fault equivalent plastic strain for $\eta = 36$ GPa s, $h = 0$ GPa, $c = 50$ MPa after the first, second, eight and eighteenth rupture events. The magnitude and off-fault extent (additional ~ 100 m per rupture) of plastic strain increases at an approximately constant rate with each rupture during the first 18 events.

Fig. 7(b) shows results from considering rate-independent plasticity with hardening parameter $h = 20$ GPa and cohesion $c = 50$ MPa. Plastic response occurs during the first event when the rupture reaches approximately 3 km depth, but has only a slight influence on slip above this depth. During the first rupture, a small slip deficit emerges above ~ 1 km depth. Because hardening causes the yield surface to expand, the response during subsequent events is effectively elastic and the slip deficit remains largely unchanged. Fig. 7(c) shows results from a viscoplastic simulation (without hardening) with $\eta = 36$ GPa s and $c = 50$ MPa. The slip deficit in the upper 3 km increases with subsequent ruptures, and after the tenth event, the slip deficit at the surface is approximately 2 m.

To assess the sensitivity to viscosity, we decrease η from 36 to 28 GPa s, seen in Fig. 8(a). The slip deficit in the upper 3 km also increases with subsequent rupture, and after the 10th event the slip deficit at the surface is approximately 3 m, suggesting that the slip deficit will increase at a faster rate for lower values of η for the viscoplastic model without hardening. Fig. 8(b) shows results from combined viscoplastic and hardening effects. For $\eta = 36$ GPa s, $h = 20$ GPa and $c = 50$ MPa, the slip deficit increases with each rupture, but at a decreasing rate, and reaches a limiting value of ~ 1 m.

Decreasing the cohesion to 40 MPa, as shown in Fig. 8(c), generates a larger slip deficit (approximately 3.5 m at the surface after the 10th event) than the analogous simulation in Fig. 8(b), although with hardening present this deficit also saturates after several ruptures.

For the values we considered, cohesion determines the depth at which plastic response occurs during rupture (confined to about 1–2 km below Earth's surface). Fig. 9 illustrates the evolution in off-fault equivalent plastic strain for the rate-independent simulation from Fig. 7(a), during the first, second, eighth and eighteenth events. The first event generates plastic strain at depths above ~ 1 km and off the fault to about 200 m at the surface. The maximum value at the fault surface is approximately 0.7 millistrain and little increase in either extent or magnitude occurs after the first event. Fig. 10 is the analogous figure for the viscoplastic model without hardening from Fig. 7(b). The first event generates a maximum

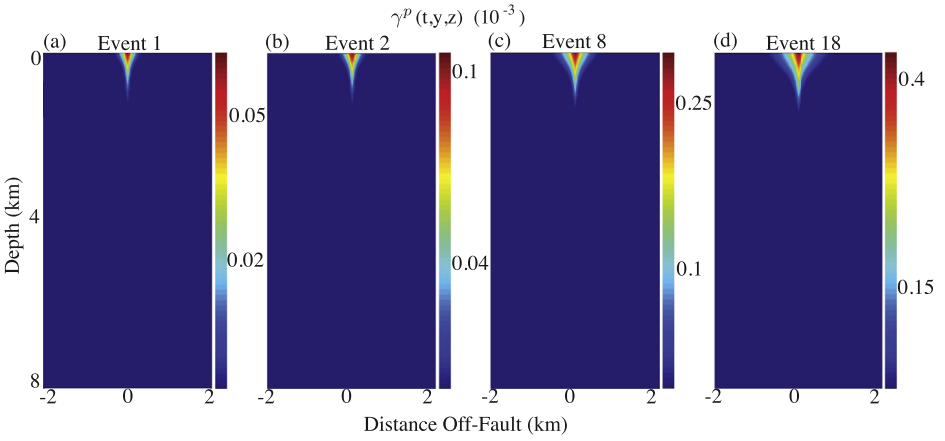

Fig. 11. Off-fault equivalent plastic strain for $\eta = 36$ GPa s, $h = 20$ GPa, $c = 50$ MPa after the first, second, eight and eighteenth rupture events. The magnitude and off-fault extent (~ 100 m during first rupture only) of plastic strain increases at an approximately decreasing rate with each rupture. After 18 events, the extent has saturated at < 1 km at the surface.

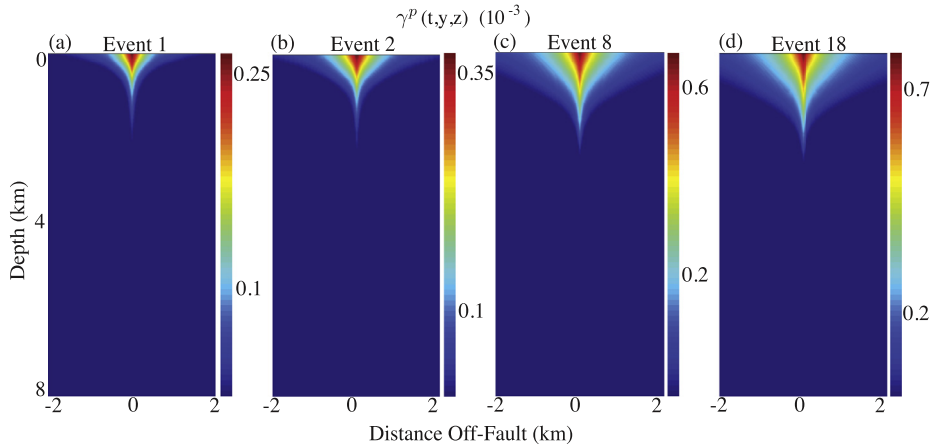

Fig. 12. Off-fault equivalent plastic strain for $\eta = 36$ GPa s, $h = 20$ GPa, $c = 40$ MPa after the first, second, eight and eighteenth rupture events. The magnitude and off-fault extent (~ 1 km during first rupture only) of plastic strain increases at an approximately decreasing rate with each rupture. After 18 events, the extent has begun to saturate near 2 km.

value of 0.06 millistrain at the fault surface, extending out to approximately 300 m and to a depth of ~ 1 km. During all subsequent events the maximum value of plastic strain increases.

Adding hardening to the viscoplastic model decreases the magnitude and extent of additional plastic strain with each rupture, see Fig. 11, so that by the eighteenth rupture, the distribution remains relatively unchanged by subsequent events. Fig. 12 illustrates the effect of a decrease in cohesion (from 50 to 40 MPa) which effectively lowers the yield stress so that plastic straining occurs at lower depths compared to previous simulations. Compared to the results shown in Fig. 11, a decrease in cohesion increases the depth of plastic strain from 1 to 2 km during the first event. In addition, a decrease in cohesion generates more plastic strain and with greater extent. By the eighteenth event, plastic strain extends beyond 2 km at the surface.

The amount of tectonic offset accommodated by plastic strain, $u^p(t, z)$, can be computed by integrating the off-fault plastic strain, namely

$$u^p(t,z) = 2\int_0^{L_y} \gamma^p_{xy}(t,y,z)\, dy. \tag{101}$$

At the surface $z = 0$, the time history of u^p is plotted in Fig. 13 and illustrates how much tectonic offset is accommodated by inelastic deformation for different plasticity models. In particular, when rate-independent plasticity with hardening is used (cyan), the amount of offset due to inelastic deformation is about 0.2 m after the first event and increases almost negligibly after the first event. If a viscoplastic relaxation is added (green), however, the amount of offset is lower during the first event, but increases with each rupture, reaching approximately 0.2 m after ~ 10 events. An increasing amount of offset accommodated by inelastic deformation occurs with each rupture for the viscoplastic models without hardening

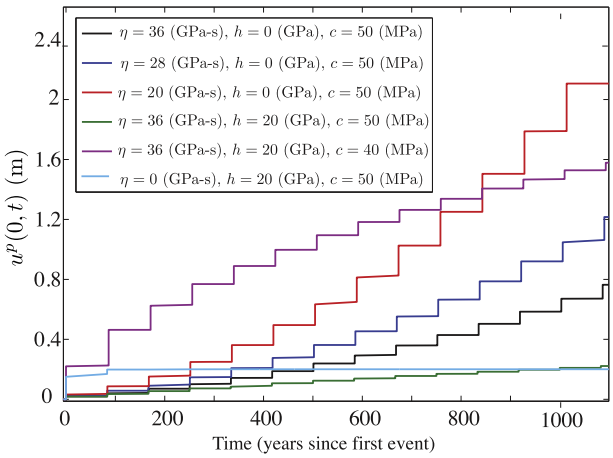

Fig. 13. Time history of integrated plastic strain at the surface showing amount of tectonic offset accommodated by inelastic deformation. (For interpretation of the references to color in this figure, the reader is referred to the web version of this article.)

(black, blue, red), with lower values of viscosity generating greater amounts of inelastic deformation. For $\eta = 20$ GPa s, for example, approximately 2 m of tectonic off-set is accommodated by inelastic strain after ~ 10 events. The rate-independent simulation with hardening present (cyan) reveals that an upper limit to the amount of inelastic deformation exists, by virtue of the fact that hardening causes in expansion of the yield surface, as illustrated in Fig. 2. The viscoplastic simulations with hardening (green and purple) show that inelastic yielding continues to occur (with greater overall amounts for lower values in cohesion), but at a decreasing rate, i.e for decreasing du^p/dt. Only the viscoplastic simulations without hardening (black, blue, red) reveal that inelastic yielding continues to occur with an increasing amount of plastic strain accruing with each event ($du^p/dt \geq 0$).

10. Discussion

We have developed a finite difference method to account for off-fault plastic response over many quasi-dynamic ruptures. The computational framework can model both rate-independent plasticity and viscoplasticity, although we found that isotropic hardening is necessary in the rate-independent model for solveability of the underlying equations. We considered a Drucker–Prager model (which reduces to von-Mises plasticity in the antiplane scenario we considered) with a depth-dependent yield stress. Numerical results were verified through convergence tests and comparisons with the solution from a finite element software package. Future work includes a deeper exploration of parameter space. For example, the inclusion of a depth dependency of the internal friction angle and cohesion (like those derived in Roten et al., 2016) will be considered. The effects of hardening and viscosity will further be explored, as our choices for these parameters were chosen primarily for efficiency of computation.

For the parameter study in this work, we found that viscosity, hardening, and cohesion all influence the extent and magnitude of off-fault plastic strain and all scenarios give rise to a shallow slip deficit. The inclusion of hardening in all models sets an upper limit on the slip deficit, which is reached at a faster rate for lower values of viscosity. The viscoplastic models with no hardening, however, give rise to the largest slip deficits which increase continuously with subsequent rupture. Our results suggest that cumulative inelastic deformation over the course of many events can account for a significant amount of tectonic offset. We found that per rupture, ~ 0.1 m of integrated plastic strain accrues, corresponding to $\sim 10\%$ of the tectonic deformation budget. Results from our model compare well to the observations of Meade et al. (2013) who estimate that 6% $\pm$ 9% of deformation occurs off of several major strike-slip faults.

Acknowledgments

We thank the editor at JMPS for handling this manuscript, as well as four anonymous reviewers for helpful comments. This work was initiated while B.A.E. was supported by the NSF under Award No. EAR-0948304 and completed with support from NSF under Award No. EAR-1547603 and by the Southern California Earthquake Center. SCEC is funded by NSF Cooperative Agreement EAR-0529922 and USGS Cooperative Agreement 07HQAG0008 (SCEC contribution number 7166).

Appendix A. The coordinate transform and penalty parameters

As stated in Section 6, we desire finer grid resolution in the domain near the fault and close to the free surface $z = 0$. Using coordinate transforms, we map the (y, z) grid in $[0, L_y] \times [0, L_z]$ with unequally spaced nodes, to a computational

domain $(\xi_1, \xi_2) \in [0, 1] \times [0, 1]$ with equal grid spacings ($N_{\xi_1} + 1$ and $N_{\xi_2} + 1$ grid points in each direction, with $\Delta\xi_1 = 1/N_{\xi_1}$, $\Delta\xi_2 = 1/N_{\xi_2}$). We let $N = (N_{\xi_1} + 1)(N_{\xi_2} + 1)$. The mapping is given by

$$y = \ell_Y \tan(\tan^{-1}(L_y/\ell_Y)\xi_1) \tag{A.1a}$$

$$z = \ell_Z \tan(\tan^{-1}(L_z/\ell_Z)\xi_2). \tag{A.1b}$$

Parameters ℓ_Y, $\ell_Z > 0$ control the strength to which nodes are clustered near the fault and surface (respectively). The mapping (A.1) is invertible, with $\frac{\partial y}{\partial \xi_1}, \frac{\partial z}{\partial \xi_2} > 0$. The Jacobian J of the transformation is

$$J = \begin{bmatrix} \dfrac{\partial y}{\partial \xi_1} & 0 \\ 0 & \dfrac{\partial z}{\partial \xi_2} \end{bmatrix} \tag{A.2}$$

with determinant $|\mathbf{J}| = \frac{\partial \mathbf{y}}{\partial \boldsymbol{\xi}_1} \otimes \frac{\partial \mathbf{z}}{\partial \boldsymbol{\xi}_2}$ where $\frac{\partial \mathbf{y}}{\partial \boldsymbol{\xi}_1}$ denotes the diagonal coefficient matrix, and $\frac{\partial \mathbf{y}}{\partial \boldsymbol{\xi}_1}^{-1}$ is its inverse (reciprocals along the diagonal). Using the notation introduced in Section 6, the SBP-SAT discretization of (33) on the computational domain is given by

$$\mathbf{0} = \mathbf{D}^{\mathbf{a}_{11}}_{2\xi_1}\mathbf{du} + \mathbf{D}_{\xi_1}\mathbf{a}_{12}\mathbf{D}_{\xi_2}\mathbf{du} + \mathbf{D}_{\xi_2}\mathbf{a}_{21}\mathbf{D}_y\mathbf{du} + \mathbf{D}^{\mathbf{a}_{22}}_{2\xi_2}\mathbf{du} + \tilde{\mathbf{P}}_L + \tilde{\mathbf{P}}_R + \tilde{\mathbf{P}}_T + \tilde{\mathbf{P}}_B, \tag{A.3}$$

where the SAT penalty vectors enforcing boundary conditions (41) are

$$\tilde{\mathbf{P}}_L = \mathbf{H}^{-1}_{\xi_1}(\boldsymbol{\alpha}_L + \beta\mathbf{H}^{-1}_{\xi_2}(-\mathbf{a}_{11}\mathbf{S}_{\xi_1} - \mathbf{a}_{12}\mathbf{D}_{\xi_2})^T)\mathbf{H}_{\xi_2}\mathbf{E}_0(\mathbf{du}_L - \mathbf{dg}_L) \tag{A.4a}$$

$$\tilde{\mathbf{P}}_R = \mathbf{H}^{-1}_{\xi_1}(\boldsymbol{\alpha}_R + \beta\mathbf{H}^{-1}_{\xi_2}(\mathbf{a}_{11}\mathbf{S}_{\xi_1} + \mathbf{a}_{12}\mathbf{D}_{\xi_2})^T)\mathbf{H}_{\xi_2}\mathbf{E}_N(\mathbf{du}_R - \mathbf{dg}_R) \tag{A.4b}$$

$$\tilde{\mathbf{P}}_T = -\mathbf{H}^{-1}_{\xi_2}(\mathbf{I}_{\xi_1} \otimes \mathbf{E}_0)\left(\left[-\mathbf{a}_{22}\mathbf{S}_{\xi_2}\mathbf{du} - \mathbf{a}_{21}\mathbf{D}_{\xi_1}\mathbf{du}\right]_T - \tilde{\mathbf{dg}}_T\right) \tag{A.4c}$$

$$\tilde{\mathbf{P}}_B = -\mathbf{H}^{-1}_{\xi_2}(\mathbf{I}_{\xi_1} \otimes \mathbf{E}_N)\left(\left[\mathbf{a}_{22}\mathbf{S}_{\xi_2}\mathbf{du} + \mathbf{a}_{21}\mathbf{D}_{\xi_1}\mathbf{du}\right]_B - \tilde{\mathbf{dg}}_B\right) \tag{A.4d}$$

where the modified boundary data are

$$\tilde{\mathbf{dg}}_T = \frac{\partial \mathbf{y}}{\partial \boldsymbol{\xi}_1}\mathbf{dg}_T \tag{A.5a}$$

$$\tilde{\mathbf{dg}}_B = \frac{\partial \mathbf{y}}{\partial \boldsymbol{\xi}_1}\mathbf{dg}_B. \tag{A.5b}$$

The modified diagonal coefficient matrices in (A.4) are

$$\mathbf{a}_{11} = \mathbf{C}^{ep}_{11}\left(\frac{\partial \mathbf{y}}{\partial \boldsymbol{\xi}_1}^{-1} \otimes \frac{\partial \mathbf{z}}{\partial \boldsymbol{\xi}_2}\right) \tag{A.6a}$$

$$\mathbf{a}_{12} = \mathbf{C}^{ep}_{12} \tag{A.6b}$$

$$\mathbf{a}_{21} = \mathbf{C}^{ep}_{21} \tag{A.6c}$$

$$\mathbf{a}_{22} = \mathbf{C}^{ep}_{22}\left(\frac{\partial \mathbf{y}}{\partial \boldsymbol{\xi}_1} \otimes \frac{\partial \mathbf{z}}{\partial \boldsymbol{\xi}_2}^{-1}\right) \tag{A.6d}$$

correspond to the moduli

$$a_{11} = C^{ep}_{11}\frac{\partial \xi_1}{\partial y} \tag{A.7a}$$

$$a_{12} = C^{ep}_{12} \tag{A.7b}$$

$$a_{21} = C^{ep}_{21} \tag{A.7c}$$

$$a_{22} = C^{ep}_{22}\frac{\partial \xi_2}{\partial z} \tag{A.7d}$$

of the transformed (continuous) problem, and we use the notation $a_{11_{i,j}} = a_{11}(y_j, z_i)$ as in Section 6.

Letting

$$\bar{\mathbf{A}} = \begin{bmatrix} \mathbf{a}_{11} & \mathbf{a}_{12} \\ \mathbf{a}_{21} & \mathbf{a}_{22} \end{bmatrix}, \tag{A.8}$$

symmetry of $\bar{\mathbf{A}}$ follows that of the 2×2 matrix $\bar{C}^{ep}$ given by (34). That $\bar{\mathbf{A}}$ is positive-definite also follows from $\bar{C}^{ep}$: Express $\bar{\mathbf{A}}$ via the Schur decomposition $\bar{\mathbf{A}}=\mathbf{X}^T\mathbf{S}\mathbf{X}$, where

$$\mathbf{S}=\begin{bmatrix}\mathbf{a_{11}} & \mathbf{0}\\ \mathbf{0} & \mathbf{a}_{22}-\mathbf{a}_{21}\mathbf{a}_{11}^{-1}\mathbf{a}_{12}\end{bmatrix} \tag{A.9}$$

and

$$\mathbf{X}=\begin{bmatrix}\mathbf{I} & \mathbf{a}_{11}^{-1}\mathbf{a}_{12}\\ \mathbf{0} & \mathbf{I}\end{bmatrix}. \tag{A.10}$$

Since $\mathbf{S}$ is a diagonal matrix, its eigenvalues lie along the diagonal. Positive-definiteness of $\bar{C}^{ep}$ guarantees that each element along the diagonal of $\mathbf{C}_{11}^{ep}$ is positive and the transformation (A.1) maintains that the diagonal matrix $\mathbf{a}_{11}$ has positive elements. The diagonal matrix $\mathbf{a}_{22}-\mathbf{a}_{21}\mathbf{a}_{11}^{-1}\mathbf{a}_{12}=(\frac{\partial \mathbf{y}}{\partial \boldsymbol{\xi}_1}\otimes\frac{\partial \mathbf{z}}{\partial \boldsymbol{\xi}_2}^{-1})[\mathbf{C}_{11}^{ep}]^{-1}(\mathbf{C}_{11}^{ep}\mathbf{C}_{22}^{ep}-\mathbf{C}_{12}^{ep}\mathbf{C}_{21}^{ep})$ has positive elements by construction of the mapping and positive-definiteness of $\bar{C}^{ep}$. Thus positive-definiteness of $\bar{\mathbf{A}}$ follows from that of $\mathbf{S}$ by the Sylvester Law of Inertia (Golub and Van Loan, 2013).

Applying the energy method to (A.3) and a proper choice of penalty parameters (given shortly) yields $\frac{d}{dt}\mathbf{dE}\le 0$, where

$$\mathbf{dE}=\frac{1}{2}\mathbf{dU}^T(\mathbf{H}_{\xi_1}\otimes\mathbf{H}_{\xi_2})\bar{\mathbf{A}}\mathbf{dU}+\frac{1}{2}\mathbf{du}^T(\mathbf{R}_{\xi_1}^{\mathbf{a}_{11}}\otimes\mathbf{H}_{\xi_2})\mathbf{du}+\frac{1}{2}\mathbf{du}^T(\mathbf{H}_{\xi_1}\otimes\mathbf{R}_{\xi_2}^{\mathbf{a}_{22}})\mathbf{du}+U_1+U_2, \tag{A.11}$$

where $\mathbf{dU}=[\mathbf{D}_{\xi_1}\mathbf{du}\ \mathbf{D}_{\xi_2}\mathbf{du}]^T$. U_1 and U_2 are non-negative quantities that that arise from the weak enforcement of Dirichlet conditions, detailed shortly.

Note that uniform grid spacing, as considered in Section 6, is the special case $\ell_Y,\ \ell_Z\to\infty$ and the transformation merely scales the overall size of the domain. In the case of uniform grid spacing, $\bar{\mathbf{A}}=\bar{\mathbf{C}}^{ep}$. The stability results of Section 6 are thus a special case of the results here.

The penalty parameters in(A.4) are derived in Virta and Mattsson (2014) and given here. The $N\times N$ diagonal coefficient matrix $\mathbf{a}_{11}$ has j, k^{th} entry $\mathbf{a}_{11_{j,k}}$. Virta and Mattsson (2014) find that penalty parameter $\beta=-1$, and penalty (diagonal) matrices $\boldsymbol{\alpha}_L$, $\boldsymbol{\alpha}_R$ have components obtained by first defining diagonal matrices $\mathbf{b}_{1L}$, $\mathbf{b}_{1R}$, $\mathbf{b}_{2L}$ and $\mathbf{b}_{2R}$ which have components

$$b_{1L_{j,j}}=\beta_p(\Delta\xi_1)\lambda_{L_j}/(a_{11_{j,1}})^2 \tag{A.12a}$$

$$b_{1R_{j,j}}=\beta_p(\Delta\xi_1)\lambda_{R_j}/(a_{11_{j,N_{\xi_1}}})^2 \tag{A.12b}$$

$$b_{2L_{j,j}}=\delta_p(\Delta\xi_1)\lambda_{j,1}/(a_{22_{j,1}})^2 \tag{A.12c}$$

$$b_{2R_{j,j}}=\delta_p(\Delta\xi_1)\lambda_{j,N_{\xi_1}}/(a_{22_{j,N_{\xi_1}}})^2 \tag{A.12d}$$

along the diagonal, where $\beta_p=36/99$ and $\delta_p=1/2$ (for the second order operators we consider),

$$\lambda_{L_j}=\min(\lambda_{j,0},\lambda_{j,1}),\ j=0,\dots,N_{\xi_2} \tag{A.13a}$$

$$\lambda_{R_j}=\min(\lambda_{j,N_{\xi_1}-1},\lambda_{j,N_{\xi_1}}),\ j=0,\dots,N_{\xi_2}, \tag{A.13b}$$

and

$$\lambda_{j,k}=\frac{1}{2}\left(a_{11_{j,k}}+a_{22_{j,k}}-\sqrt{(a_{11_{j,k}}-a_{22_{j,k}})^2+4(a_{12_{j,k}})^2}\right). \tag{A.14a}$$

The positive quantities given in the incremental internal energy are

$$U_1=\mathbf{U}_L^T\mathbf{H}_3\mathbf{T}_L\mathbf{U}_L \tag{A.15a}$$

$$U_2=\mathbf{U}_R^T\mathbf{H}_3\mathbf{T}_R\mathbf{U}_R \tag{A.15b}$$

for vectors

$$\mathbf{U}_L=[\mathbf{du_L}^T\quad(\mathbf{B}^{\mathbf{a}_{11}}\mathbf{S}_{\xi_1}\mathbf{du})_L^T\quad(\mathbf{a}_{12}\mathbf{D}_{\xi_1}\mathbf{du})_L^T]^T, \tag{A.16a}$$

$$\mathbf{U}_R=[\mathbf{du_R}^T\quad(\mathbf{B}^{\mathbf{a}_{11}}\mathbf{S}_{\xi_1}\mathbf{du})_R^T\quad(\mathbf{a}_{12}\mathbf{D}_{\xi_1}\mathbf{du})_R^T]^T, \tag{A.16b}$$

$$\mathbf{H}_3=\mathrm{diag}([\mathbf{H}_{\xi_1}\otimes\mathbf{H}_{\xi_2},\quad\mathbf{H}_{\xi_1}\otimes\mathbf{H}_{\xi_2},\quad\mathbf{H}_{\xi_1}\otimes\mathbf{H}_{\xi_2}]). \tag{A.16c}$$

Matrix $\mathbf{B}^{\mathbf{a}_{11}}$ is a coefficient matrix for $\mathbf{a}_{11}$ formed in a special way (see Virta and Mattsson, 2014 for details). Matrices

$$\mathbf{T}_L=\begin{bmatrix}-\boldsymbol{\alpha}_L & -\mathbf{1} & -\mathbf{1}\\ -\mathbf{1} & \mathbf{b}_{1R} & \mathbf{0}\\ -\mathbf{1} & \mathbf{0} & \mathbf{b}_{2R}\end{bmatrix} \tag{A.17a}$$

and

$$\mathbf{T}_R = \begin{bmatrix} -\boldsymbol{\alpha}_R & -\mathbf{1} & -\mathbf{1} \\ -\mathbf{1} & \mathbf{b}_{1L} & \mathbf{0} \\ -\mathbf{1} & \mathbf{0} & \mathbf{b}_{2L} \end{bmatrix} \tag{A.18a}$$

are shown to be positive semi-definite if

$$\alpha_{L_{j,j}} \leq -\frac{1}{b_{1R_{j,j}}} - \frac{1}{b_{2R_{j,j}}}, \quad j = 0, \ldots, N_{\xi_2} \tag{A.19a}$$

$$\alpha_{R_{j,j}} \leq -\frac{1}{b_{1R_{j,j}}} - \frac{1}{b_{2R_{j,j}}}, \quad j = 0, \ldots, N_{\xi_2} \tag{A.19b}$$

(Virta and Mattsson, 2014).

Appendix B. The consistent tangent moduli

The consistent tangent moduli for both rate-independent and viscoplasticity are derived here simultaneously. Applying a backward-Euler discretization to the flow rule (19), we have

$$\sigma_{ij}^{n+1} = C_{ijkl}(\epsilon_{kl}^{n+1} - \epsilon_{kl}^{p,n+1}) = C_{ijkl}(\epsilon_{kl}^{n+1} - \epsilon_{kl}^{p,n} - d\lambda^{n+1}\frac{s_{kl}^{n+1}}{2\bar{\tau}^{n+1}}). \tag{B.1}$$

The consistent elastoplastic tangent stiffness tensor $\mathcal{C}_{ijkl}^{ep,n+1} = \frac{\partial \sigma_{ij}^{n+1}}{\partial \epsilon_{kl}^{n+1}}$ can be computed by first defining a few terms. Following Simo and Hughes (1998), let $n_{ij} = s_{ij}/2\bar{\tau}$. Then

$$\frac{\partial n_{ij}}{\partial s_{kl}} = \frac{1}{\bar{\tau}}\left[\frac{1}{2}I_{ijkl} - n_{ij}n_{kl}\right], \tag{B.2}$$

where the fourth order, symmetric identity tensor

$$I_{ijkl} = \frac{1}{2}\left[\delta_{ik}\delta_{jl} + \delta_{il}\delta_{jk}\right]. \tag{B.3}$$

It is a quick exercise to show that

$$n_{ij}^{*,n+1} = n_{ij}^{n+1}, \tag{B.4}$$

and therefore we have

$$\frac{\partial \bar{\tau}^{*,n+1}}{\partial \epsilon_{kl}^{n+1}} = \frac{1}{\bar{\tau}^{*,n+1}}\sigma_{kl}^{*,n+1}\mu = 2\mu n_{kl}^{*,n+1} = 2\mu n_{kl}^{n+1}. \tag{B.5}$$

Next, recall the plastic consistency condition (71), which can be expressed

$$\bar{\tau}^{*,n+1} - \sigma_Y - h\gamma_p^n = (\eta/dt + \mu + h)d\lambda^{n+1} \tag{B.6}$$

where the rate-independent case is obtained by taking $\eta = 0$. Taking the partial derivative of (B.6) yields

$$\frac{\partial \bar{\tau}^{*,n+1}}{\partial \epsilon_{kl}^{n+1}} = (\eta/dt + \mu + h)\frac{\partial d\lambda^{n+1}}{\partial \epsilon_{kl}^{n+1}}. \tag{B.7}$$

Re-arranging (B.7) and substituting in (B.5) yields

$$\frac{\partial \Delta\lambda^{n+1}}{\partial \epsilon_{kl}^{n+1}} = \frac{2\mu}{\eta/dt + \mu + h}n_{kl}^{n+1}. \tag{B.8}$$

Also note that we have,

$$C_{ijmn}\frac{\partial s_{mn}}{\partial \epsilon_{kl}} = 2\mu\frac{\partial s_{ij}}{\partial \epsilon_{kl}}. \tag{B.9}$$

Therefore

$$\frac{\partial n_{ij}^{n+1}}{\partial \epsilon_{kl}^{n+1}} = \frac{\partial n_{ij}^{*,n+1}}{\partial \epsilon_{kl}^{n+1}} = \frac{\partial n_{ij}^{*,n+1}}{\partial \sigma_{mn}^{*,n+1}}\frac{\partial \sigma_{mn}^{*,n+1}}{\partial \epsilon_{kl}^{n+1}} = \frac{\partial n_{ij}^{*,n+1}}{\partial \sigma_{mn}^{*,n+1}}C_{mnkl} = 2\mu\frac{\partial n_{ij}^{*,n+1}}{\partial \sigma_{kl}^{*,n+1}} = 2\mu\frac{\partial n_{ij}^{n+1}}{\partial s_{kl}^{n+1}}. \tag{B.10}$$

When plastic straining is occurring (i.e. when $\lambda > 0$), we can compute the consistent elastoplastic tangent stiffness tensor by taking the partial derivative of Eq. (B.1)

$$\mathcal{C}^{ep,n+1}_{ijkl} = \frac{\partial \sigma^{n+1}_{ij}}{\partial \epsilon^{n+1}_{ij}} = C_{ijkl} - \frac{\partial d\lambda^{n+1}}{\partial \epsilon^{n+1}_{kl}} \mu n^{n+1}_{ij} - d\lambda^{n+1} \mu \frac{\partial n^{n+1}_{ij}}{\partial \epsilon^{n+1}_{kl}} \tag{B.11}$$

$$= C_{ijkl} - \frac{2\mu}{\eta/dt + \mu + h} n^{n+1}_{kl} 2\mu n^{n+1}_{ij} - d\lambda^{n+1} 2\mu \left(2\mu \frac{\partial n^{n+1}_{ij}}{\partial s^{n+1}_{kl}} \right) \tag{B.12}$$

$$= C_{ijkl} - \frac{4\mu^2}{\eta/dt + \mu + h} n^{n+1}_{kl} n^{n+1}_{ij} - d\lambda^{n+1} 4\mu^2 \frac{1}{\bar{\tau}^{n+1}} \left[\frac{1}{2} I_{ijkl} - n^{n+1}_{ij} n^{n+1}_{kl} \right]. \tag{B.13}$$

and the specific case for antiplane motion given in (73)–(75) for rate-independent plasticity, and (78)–(80) for viscoplasticity follow, using the notation $\mathcal{C}^{ep}_{11} = \mathcal{C}^{ep}_{xyxy}$, $\mathcal{C}^{ep}_{22} = \mathcal{C}^{ep}_{xzxz}$, $\mathcal{C}^{ep}_{12} = \mathcal{C}^{ep}_{xyxz}$, $\mathcal{C}^{ep}_{21} = \mathcal{C}^{ep}_{xzxy}$.

Appendix C. Mesh refinement

We double the number of grid points used in the simulation shown in Fig. 7(c) with $\eta = 36$, $h = 0$ and $c = 50$ MPa, see Fig. C.14. Although a bit more slip occurs with each rupture when mesh refining (note last event for each simulation, for example), the results appear qualitatively similar.

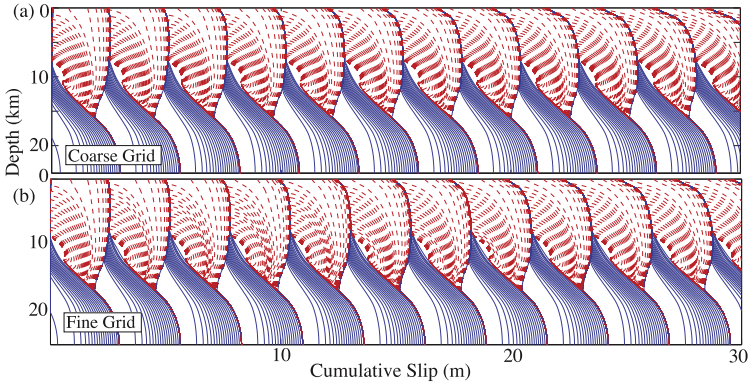

Fig. C.14. Snapshots of cumulative slip profiles plotted at 5-a intervals during interseismic period when $\max(V) \leq 1$ mm/s and dashed red profiles plotted at 1 s intervals during quasi-dynamic rupture for $\eta = 36$ GPa s, $h = 0$ GPa, $c = 50$ MPa for (a) the coarse grid simulation from Fig. 7(c) (plotted again for ease of comparison) and (b) results when using twice the number of grid points. (For interpretation of the references to color in this figure legend, the reader is referred to the web version of this article.)

References

Aagaard, B.T., Knepley, M.G., Williams, C.A., 2013. A domain decomposition approach to implementing fault slip infinite-element models of quasi-static and dynamic crustal deformation. J. Geophy. Res. 118, 3059–3079. doi:10.1002/jgrb.50217.

Allison, K.L., Dunham, E.M., 2017. Earthquake cycle simulations with rate-and-state friction and nonlinear Maxwell rheology. Tectonophysics 1–50. (submitted for publication).

Ampuero, J.-P., Rubin, A.M., 2008. Earthquake nucleation on rate and state faults: aging and slip laws. J. Geophy. Res. 113, 1–21. doi:10.1029/2007JB005082.

Barbot, S., Lapusta, N., Avouac, J.-P., 2012. Under the hood of the earthquake machine: toward predictive modeling of the seismic cycle. Science 336, 707–710. doi:10.1126/science.1218796.

Ben-Zion, Y., Sammis, C., 2011. Brittle deformation of solid and granular materials with applications to mechanics of earthquakes and faults. Pure Appl. Geophys. 168, 2147–2149. doi:10.1007/s00024-011-0418-8.

Bower, A.F., 2010. Applied Mechanics of Solids. Taylor and Francis Group, LLC, CRC Press, Boca Raton, FL.

Chen, W.F., Han, D.J., 1988. Plasticity for Structural Engineers, first ed. Springer-Verlag, New York. 1–606.

Chester, F.M., Evans, J.P., Biegel, R.L., 1993. Internal structure and weakening mechanisms of the San Andreas Fault. J. Geophy. Res. 98, 771–786. doi:10.1029/92JB01866.

Chester, F.M., Logan, J.M., 1986. Implications for mechanical properties of brittle faults from observations of the punchbowl fault zone, California. Pure Appl. Geophys. 124, 79–106. doi:10.1007/BF00875720.

de Souza Neto, E.A., Perić, D., Owen, D.R.J., 2008. Computational Methods for Plasticity, first ed. John Wiley & Sons Ltd, United Kingdom. 1–791.DeSouza

Dieterich, J.H., 1979. Modeling of rock friction: 1. Experimental results and constitutive equations. J. Geophy. Res. 84, 2161–2168. doi:10.1029/JB084iB05p02161.

Drucker, D.C., 1959. A definition of a stable inelastic material. J. Appl. Mech. ASME 26, 101–195.

Dunham, E.M., Belanger, D., Cong, L., Kozdon, J.E., 2011a. Earthquake ruptures with strongly rate-weakening friction and off-fault plasticity, part 1: planar faults. Bull. Seismol. Soc. Am. 101 (5), 2296–2307. doi:10.1785/0120100075.

Dunham, E.M., Belanger, D., Cong, L., Kozdon, J.E., 2011b. Earthquake ruptures with strongly rate-weakening friction and off-fault plasticity, part 2: nonplanar faults. Bull. Seismol. Soc. Am. 101 (5), 2308–2322. doi:10.1785/0120100076.
Dunne, F., Petrinic, N., 2006. Introduction to Computational Plasticity, first ed. Oxford University Press, New York. 1–242
Erickson, B.A., Dunham, E.M., 2014. An efficient numerical method for earthquake cycles in heterogeneous media: alternating subbasin and surface-rupturing events on faults crossing a sedimentary basin. J. Geophy. Res. 119, 1–27. doi:10.1002/2013JB010614.
Faulkner, D.R., Jackson, C.A.L., Lunn, R.J., Schlische, R.W., Shipton, Z.K., Wibberley, C.A.J., Withjack, M.O., 2010. A review of recent developments concerning the structure, mechanics and fluid flow properties of fault zones. J. Struct. Geol. 32 (11), 1557–1575. doi:10.1016/j.jsg.2010.06.009.
Gabriel, A.-A., Ampuero, J.-P., Dalguer, L.A., Mai, P.M., 2013a. Source properties of dynamic rupture pulses with off-fault plasticity. J. Geophys. Res. 118 (8), 4117–4126. doi:10.1002/jgrb.50213.
Gabriel, A.-A., Ampuero, J.-P., Dalguer, L.A., Mai, P.M., 2013b. The transition of dynamic rupture styles in elastic media under velocity-weakening friction. J. Geophys. Res. 117, 1–20. doi:10.1029/2012JB009468.
Golub, G.H., Van Loan, C.F., 2013. Matrix Computations, fourth ed. JHU Press, Baltimore.
Gustafsson, B., 2008. High Order Difference Methods for Time Dependent PDE. Springer-Verlag, Berlin doi:10.1007/978-3-540-74993-6.
Horn, R.A., Johnson, C.R., 1985. Matrix Analysis. Cambridge University Press, New York.
Jain, S.K., 2008. Introduction to Theories of Plasticity, Part 1: Stress-Strain Relations. Engineering Publications, Virginia.
Johnson, K.M., Segall, P., 2004. Viscoelastic earthquake cycle models with deep stress-driven creep along the San Andreas Fault system. J. Geophy. Res. 109, 1–19. doi:10.1029/2004JB003096.
Kaneko, Y., Ampuero, J.-P., Lapusta, N., 2011. Spectral-element simulations of long-term fault slip: effect of low-rigidity layers on earthquake-cycle dynamics. J. Geophys. Res. 116, 1–18. B10313, doi: 10.1029/2011JB008395.
Kaneko, Y., Fialko, Y., 2011. Shallow slip deficit due to large strike-slip earthquakes in dynamic rupture simulations with elasto-plastic off-fault response. Geophys. J. Int. 186, 1389–1403. doi:10.1111/j.1365-246X.2011.05117.x.
Kreiss, H.-O., Scherer, G., 1974. Finite element and finite difference methods for hyperbolic partial differential equations. In: Mathematical Aspects of Finite Elements in Partial Differential Equations, pp. 195–212. doi:10.1016/B978-0-12-208350-1.50012-1.
Kreiss, H.-O., Scherer, G., 1977. On the Existence of Energy Estimates for Difference Approximations for Hyperbolic Systems. Technical Report, Department of Scientific Computing, Uppsala University.
Lapusta, N., Rice, J.R., Ben-Zion, Y., Zheng, G., 2000. Elastodynamic analysis for slow tectonic loading with spontaneous rupture episodes on faults with rate-and-state dependent friction. J. Geophy. Res. 105, 23765–23789. doi:10.1029/2000JB900250.
Ma, S., Andrews, D.J., 2010. Inelastic off-fault response and three-dimensional earthquake rupture dynamics on a strike-slip fault. J. Geophys. Res. 115, 1–16. doi:10.1029/2009JB006382.
Marone, C., 1998. Laboratory-derived friction laws and their application to seismic faulting. Ann. Rev. Earth Planet. Sci. 26, 643–696. doi:10.1146/annurev.earth.26.1.643.
Mattsson, K., 2011. Summation by parts operators for finite difference approximations of second-derivatives with variable coefficients. J. Sci. Comput. 51, 650–682. doi:10.1007/s10915-011-9525-z.
Mattsson, K., Nordström, J., 2004. Summation by parts operators for finite difference approximations of second derivatives. J. Comput. Phys. 199, 503–540. doi:10.1016/j.jcp.2004.03.001.
Mazzoni, S., McKenna, F., Scott, M.H., Fenves, G.L., 2009. Open System for Earthquake Engineering Simulation User Manual. University of California, Berkeley.
Meade, B.J., Klinger, Y., Hetland, E.A., 2013. Inference of multiple earthquake-cycle relaxation timescales from irregular geodetic sampling of interseismic deformation. Bull. Seismol. Soc. Am. 103, 2824–2835. doi:10.1785/0120130006.
Mitchell, T.M., Faulkner, D.R., 2009. The nature and origin of off-fault damage surrounding strike-slip fault zones with a wide range of displacements: a field study from the Atacama fault zone, Northern Chile. J. Struct. Geol. 31 (8), 802–816. doi:10.1016/j.jsg.2009.05.002.
Nordström, J., Mattsson, K., Swanson, C., 2007. Boundary conditions for a divergence free velocity–pressure formulation of the Navier–Stokes equations. J. Comput. Phys. 225, 874–890. doi:10.1016/j.jcp.2007.01.010.
Perzyna, P., 1966. Fundamental problems in viscoplasticity. Adv. Appl. Mech. 9, 243–377. doi:10.1016/S0065-2156(08)70009-7.
Perzyna, P., 1971. Thermodynamic theory of viscoplasticity. Adv. Appl. Mech. 11, 313–354. doi:10.1016/S0065-2156(08)70345-4.
Ranjith, K., 2008. Dynamic anti-plane sliding of dissimilar anisotropic linear elastic solids. Int. J. Solids Struct. 45, 4211–4221. doi:10.1016/j.ijsolstr.2008.03.002.
Rice, J.R., 1992. Fault stress states, pore pressure distributions and the weakness of the san andreas fault. In: Evans, B., Wong, T.-F. (Eds.), Fault Mechanics and Transport Properties of Rock. Academic, San Diego, Calif, pp. 475–503.
Rice, J.R., 1993. Spatio-temporal complexity of slip on a fault. J. Geophy. Res. 98, 9885–9907. doi:10.1029/93JB00191.
Roache, P., 1998. Verification and Validation in Computational Science and Engineering, first ed. Hermosa Publishers, Albuquerque.
Roten, D., Olsen, K.B., Day, S.M., Cui, Y., 2016. Quantification of fault zone plasticity effects with spontaneous rupture simulations. In: Proceedings of the Workshop on Best Practices in Physics-Based Fault Rupture Models for Seismic Hazard Assessment of Nuclear Installations. Vienna, pp. 18–20. November 2015, Unpublished conference paper.
Ruina, A., 1983. Slip instability and state variable friction laws. J. Geophy. Res. 88, 10359–10370. B12, doi: 10.1029/JB088iB12p10359.
Scalerandi, M., Delsanto, P.P., Chiroiu, C., Chiroiu, V., 1999. Numerical simulation of pulse propagation in nonlinear 1-D media. J. Acoust. Soc. Am. 106, 2424–2430. doi:10.1121/1.428078.
Shi, Z., Day, S.M., 2013. Rupture dynamics and ground motion from 3-D rough-fault simulations. J. Geophy. Res. 118, 1122–1141. doi:10.1002/jgrb.50094.
Shipton, Z.K., Evans, J.P., Thompson, L.B., 2005. The geometry and thickness of deformation-band fault core and its influence on sealing characteristics of deformation-band fault zones. In: Sorkabi, R., Tsuji, Y. (Eds.), Faults, Fluid Flow, and Petroleum Traps, AAPG Memoir, 85. American Association of Petroleum Geologists, Tulsa, Okla, pp. 181–195.
Simo, J.C., Hughes, T.J.R., 1998. Computational Inelasticity, first ed. Springer, New York. doi:10.1007/b98904.
Simo, J.C., Taylor, R.L., 1985. Consistent tangent operators for rate-independent elastoplasticity. Comput. Methods Appl. Mech. Eng. 48, 101–118. doi:10.1016/0045-7825(85)90070-2.
Svärd, M., Nordström, J., 2014. Review of summation-by-parts schemes for initial-boundary-value problems. J. Comput. Phys. 268, 17–38. doi:10.1016/j.jcp.2014.02.031.
Templeton, E., Rice, J.R., 2008. Off-fault plasticity and earthquake rupture dynamics: 1. Dry materials or neglect of fluid pressure changes. J. Geophys. Res. 113, 1–19. doi:10.1029/2007JB005529.
Thompson, T.B., Meade, B.J., 2016. Next generation boundary element models for earthquake science. In: Proceedings of the 2016 SCEC Annual Meeting.
Tullis, T.E., Richards-Dinger, K., Barall, M., Dietrich, J.H., Field, E.H., Heien, E.M., Kellog, L.H., Pollitz, F.F., Rundle, J.B., Sachs, M.K., Turcotte, D.L., Ward, S.N., Yikilmaz, M.B., 2012. Generic earthquake simulator. Seismol. Res. Lett. 83, 959–963. doi:10.1785/0220120093.
Virta, K., Mattsson, K., 2014. Acoustic wave propagation in complicated geometries and heterogeneous media. J. Sci. Comput. 61. doi:10.1007/s10915-014-9817-1.
Xu, S., Ben-Zion, Y., Ampuero, J.-P., 2012. Properties of inelastic yielding zones generated by in-plane dynamic ruptures: I. Model description and basic results. Geophys. J. Int. 191, 1325–1342. doi:10.1111/j.1365-246X.2012.05679.x.
Xu, S., Ben-Zion, Y., Ampuero, J.-P., 2012. Properties of inelastic yielding zones generated by in-plane dynamic ruptures: II. Detailed parameter-space study. Geophys. J. Int. 191, 1343–1360. doi:10.1111/j.1365-246X.2012.05685.x.